UNIVERSITÀ DEGLI STUDI DI PADOVA

Dipartimento di Fisica e Astronomia "Galileo Galilei"

Master Degree in Physics

Final Dissertation

Dynamic detection of the bio-molecular interaction at the surface of plasmonic nanoarrays

Thesis supervisor

Prof. Giovanni Mattei

Thesis co-supervisor

Ionut Gabriel Balasa

Candidate

Martina Russo

Academic Year 2020/2021

To Edo, my family,
MARE and Joůœūördœn

Abstract

Nanophysics and plasmonics have recently become fields of relevant interest in the world of research and, in particular, in biosensing and biochemistry. Nanoparticles of noble metals interact with incident light giving rise to the Localized Surface Plasmon Resonance (LSPR), which is a sharp peak of the extinction spectra of the nanoparticles as a result of the collective oscillation at a resonant frequency of the conduction electrons. The shape of the peak and its position strongly depend on both nano system properties, as composition, size, shape, orientation, and on the local dielectric environment. A change in the medium in which the nanoparticle is embedded is indeed detected and transduced as a distortion and shift of the peak.

This mechanism is at the basis of the biosensing application of plasmonic structures, revealing binding events of molecules to the surface or extremely small variation in concentration of substances in the proximity. For this reason, LSPR plasmonic biosensors gained great popularity in a broad range of applications, in particular as diagnostic devices able to quantitatively detect biomarker molecules. MicroRNA, among the others, are biomolecules of prominent interest associated to thumoral or other kind of diseases.

The aim of this project is to realize and test a sensitive, specific and label-free plasmonic nanobiosensor able to detect microRNA target molecules and to investigate the dynamics of the binding of the biomolecules on the surface of the optical transducers.

To accomplish this task, Au nanoprisms arrays (NPA) are chosen as reference structure, with a LSPR wavelength around 800 nm and nanofabricated via NanoSphere Lithography (NSL) and thermal evaporation deposition. A self-assembled layer of close packed polystyrene nanospheres is used as a mask for the following metal deposition via thermal evaporation. After removing the mask layer, the final pattern is an ordered hexagonal array of triangular nanoprisms. All the samples are morphologically characterized with AFM or SEM microscopy.

Post-treating procedure and functionalization protocols are employed to allow the binding of the analyte molecule to be detected to the sensor, and all the functionalization signals are detected by linear optical spectroscopy in the visible or near-infrared spectral range. Static measurements are performed to control the peak shift of the sample after each functionalization step, and dynamic measurements in a microfluidic setup allow to monitor the temporal evolution of the optical signal and to reconstruct in real-time the hybridization kinetics at the surface of the plasmonic sensor.

A $217 nm/RIU$ bulk sensitivity and $50 fMoles$ limit of detection is reached with the employed structures, indicating that both the nanofabrication and functionalization strategy are successful in the detection of analyte molecules down to low concentration limits. Of course, optimization is desirable, to push even further the sensitivity and solve challenges as for example the aspecific target binding on the sensor surface.

Another purpose of the work is to extract interesting information about the dynamics of the hybridization reaction that takes place when the analyte microRNA is bound to the surface of the nanoarray. Hybridization kinetics is studied, determining the time and affinity constants characterizing the reaction. The results obtained will prove the non-ideal behaviour of the association, laying the basis for future and advanced outlook about the building of a non-Langmuir association model able to analytically describe the bi-molecular binding system.

Contents

1 Electromagnetic Radiation Interaction with Metals **1**
1.1 Electronic and Optical Properties of Metals 1
1.1.1 Drude Model 3
1.1.2 Lorentz-Drude Model 5
1.2 Plasmon Polaritons Excitation 6
1.2.1 Volume Plasmon 6
1.2.2 Surface Plasmon Polariton 6
1.3 Localized Surface Plasmons 8
1.3.1 Quasi-static Approximation for a Single Spherical Nanoparticle . 9
1.3.2 Mie Theory 10
1.3.3 LSPR in Particle Ensembles and Hot-Spots 11

2 LSPR-Based Plasmonic Biosensors **13**
2.1 Refractive Index Sensing 14
2.1.1 Substrate Size and Shape Dependence 15
2.1.2 Performance Characteristics 16
2.2 Instrumental Optical Setup for LSPR Sensing 17
2.2.1 Microfluidic Systems 17
2.3 Functionalization Protocols 19

3 Nanofabrication of Plasmoinc Nanoprism Arrays **21**
3.1 Nanosphere Lithography 21
3.1.1 Substrate Preparation 22
3.1.2 Polystyrene Nanosphere Mask 23
3.1.3 Thermal Evaporation Deposition 24
3.2 Sample Post-treatment 26
3.2.1 Physical Techniques 27
3.2.2 Chemical Techniques 28

4 MicroRNA Biosensing **29**
4.1 Optical Measurement Setup 29
4.1.1 Data Analysis 30
4.1.2 Microfluidic Chambers 31
4.2 Functionalization Protocols 32
4.2.1 Thiols Functionalization 33
4.2.2 Probe Functionalization 34
4.2.3 Target Hybridization 34
4.3 Characterization and Sensing Performances 35
4.3.1 Microscopy Characterization 35

4.3.2 Biosensing Experiments 36
4.3.3 Biosensor Regeneration 37

5 Dynamic Biosensing **39**
5.1 Setup and Data Elaboration 40
5.2 Results and Analysis 41
5.2.1 Limit of Detection 43
5.3 Kinetics of the Hybridization 45

6 Conclusions and Outlooks **49**

Bibliography **51**

Chapter 1

Electromagnetic Radiation Interaction with Metals

1.1 Electronic and Optical Properties of Metals

Many applications of current nanotechnologies are based on nanophotonics, that is the study of the electromagnetic (EM) field interaction with nanostructures, and its prominent field of plasmonics, that investigates the same interaction between EM radiation and free electrons at the interface between a metal and a dielectric material. One of the remarkable implications is thus the possibility to confine EM fields in region whose dimensions are comparable or even smaller than the wavelength.

The electronic and optical properties of metallic nanostructures and their interaction with light can be easily studied starting from the classical EM framework of Maxwell equations and, down to the order of few nanometers, no quantum mechanical approach is needed [1].

The *complex dielectric function* $\varepsilon(\omega)$ of a metal is the physical quantity which encloses its electronic and optical properties, which are functions of the EM field frequency and of the intrinsic electronic band structure of the metal. The dielectric function can be derived starting from a theoretical model and compared with experimental values.

In general, metals show the same trend when interacting with different wavelength EM radiations: at low frequencies, up to the far-infrared region of the spectrum, metals are highly reflective, leading to the absence of EM waves propagation through them, except for a negligible penetration region called *skin depth*. The radiation penetration and following dissipation significantly increase at higher frequency region (near-infrared, visible) and finally, at ultraviolet (UV) frequencies, metals may exhibit a dielectric behavior. EM waves propagation through them is allowed, with characteristics depending on the electronic properties; noble metals, for example, show strong absorption in UV range, unlike alkali metals, almost transparent in that region.

The first step to formulate the study of the EM radiations interaction with metallic nanostructures is the set of Maxwell's equations for the EM fields:

$$\nabla \cdot \mathbf{D} = \rho_{ext} \tag{1.1a}$$

$$\nabla \cdot \mathbf{B} = 0 \tag{1.1b}$$

$$\nabla \times \mathbf{E} = -\frac{\partial \mathbf{B}}{\partial t} \tag{1.1c}$$

$$\nabla \times \mathbf{H} = \mathbf{J}_{\text{ext}} + \frac{\partial \mathbf{D}}{\partial \mathbf{t}} \tag{1.1d}$$

relating the four macroscopic fields **D** (dielectric displacement), **B** (magnetic induction), **E** (electric field) and **H** (magnetic field) to the external charge density ρ_{ext} and current density $\mathbf{J}_{\text{ext}}$. The framework is completed by the two auxiliary fields **P** (polarization) and **M** (magnetization), defined as follows:

$$\mathbf{D} = \varepsilon_0 \mathbf{E} + \mathbf{P} \tag{1.2a}$$

$$\mathbf{H} = \frac{1}{\mu_0}\mathbf{B} - \mathbf{M} \tag{1.2b}$$

where ε_0 and μ_0 are vacuum electric permittivity and magnetic permeability. Between the two field **M** and **P**, the magnetization can be neglected in the following, since in this work magnetic effect will not be considered. The polarization, on the other side, is the electric dipole moment per unit volume inside the material, and is related to the internal charge density ρ_{int} by the relation $\nabla \cdot \mathbf{P} = -\rho_{int}$; charge conservation provides:

$$\nabla \cdot \mathbf{J} = -\frac{\partial \rho_{int}}{\partial t} \qquad \Rightarrow \qquad \mathbf{J} = \frac{\partial \mathbf{P}}{\partial t}. \tag{1.3}$$

If the assumption of linear, isotropic and nonmagnetic medium is now added, it is possible to write a linear relation between the fields **D** and **E** and **B** and **H** respectively:

$$\mathbf{D} = \varepsilon_0 \varepsilon \mathbf{E} \tag{1.4a}$$

$$\mathbf{B} = \mu_0 \mu \mathbf{H} \tag{1.4b}$$

with ε and μ dielectric constant and relative permittivity of the medium respectively.

Another fundamental general relation is the one linearly linking the internal current density **J** and the electric field **E** through the conductivity σ:

$$\mathbf{J} = \sigma \mathbf{E}. \tag{1.5}$$

A correction is to be made in equations (1.4a) and (1.4b), taking into account the metals optical response dependence on the frequency, which implies a non-locality in time and space to which the previous formula can be easily extended to:

$$\mathbf{D}(\mathbf{r}, t) = \varepsilon_0 \int dt' \mathbf{dr}' \varepsilon \left(\mathbf{r} - \mathbf{r}', t - t'\right) \mathbf{E}\left(\mathbf{r}', t'\right) \tag{1.6a}$$

$$\mathbf{J}(\mathbf{r}, t) = \int dt' \mathbf{dr}' \sigma \left(\mathbf{r} - \mathbf{r}', t - t'\right) \mathbf{E}\left(\mathbf{r}', t'\right). \tag{1.6b}$$

A Fourier transform of these expressions leads to a more intuitive form with domain in the reciprocal space $(\mathbf{k}, \omega)$:

$$\mathbf{D}(\mathbf{k}, \omega) = \varepsilon_0 \varepsilon(\mathbf{k}, \omega) \mathbf{E}(\mathbf{k}, \omega) \tag{1.7a}$$

$$\mathbf{J}(\mathbf{k}, \omega) = \sigma(\mathbf{k}, \omega) \mathbf{E}(\mathbf{k}, \omega) \tag{1.7b}$$

Handling together equations (1.2a), (1.3), (1.7a) and (1.7b), a relation is derived between the dielectric function ε and the conductivity σ:

$$\varepsilon(\mathbf{k}, \omega) = 1 + \frac{i\sigma(\mathbf{k}, \omega)}{\varepsilon_0 \omega}. \tag{1.8}$$

The above relation allows to describe the electronic-optical response to the EM field interaction by means of ε or σ equivalently. Since for historical reasons conductivity is preferred at low frequencies, from now on all the theoretical treatment will be done focusing on the dielectric function ε, as the spectral range of interest of the present research is the NIR-Vis-UV one.

Moreover, in the *long wavelength limit* ($\lambda \gtrsim 100nm$), which is valid as long as the wavelength λ of the EM radiation in the medium is larger than all characteristic dimensions like electrons mean free path or the unit cell size, the assumption of *spatially local* response is fulfilled and the dielectric function can be written as $\varepsilon(\mathbf{k} = \mathbf{0}, \omega) = \varepsilon(\omega)$.

The complex dielectric function is composed by a real and an imaginary part $\varepsilon(\omega) = \varepsilon_1(\omega) + i\varepsilon_2(\omega)$, each ones dependent on the frequency. Defining the *complex refractive index* $\tilde{n}(\omega) = n(\omega) + ik(\omega)$, with n *refractive index* and k *extinction coefficient*, one can write the relations:

$$\tilde{n}(\omega) = \sqrt{\varepsilon(\omega)} \tag{1.9a}$$

$$\varepsilon_1 = n^2 - k^2 \tag{1.9b}$$

$$\varepsilon_2 = 2nk \tag{1.9c}$$

$$\alpha(\omega) = \frac{2k(\omega)\omega}{c} \tag{1.9d}$$

where α is the absorption coefficient describing the optical absorption of EM waves of an input beam of intensity I_0 inside the material through Beer's law $I(x) = I_0 e^{-\alpha x}$.

In the following sections of the chapter, two different models are introduced to derive the complex dielectric function of a metal.

1.1.1 Drude Model

Since the optical response of a metal to the interaction of an impinging EM field is enclosed inside its dielectric function $\varepsilon(\omega)$, it is interesting to build a theoretical model able to derive an expression for $\varepsilon(\omega)$ starting from consideration upon the electrons movement of the medium of interest.

To this purpose, the well known *Drude model*, known also as *free electron gas model*, was build by its author Paul Karl Ludwig Drude considering the electrons of a metal as a gas of free electrons of numerical density n moving in a fixed lattice of positive ions. As a *plasma model*, the electron-electron interaction is neglected as well as the lattice potential, while some details of the band structure are included inside the effective mass of the electron m.

The ideality assumption makes the model not the most accurate one to describe the optical response of a metal over the entire spectral range, however it gives good results and good experimental confirmation over a wide range of frequencies, which can slightly vary considering different types of metals. For example, while for alkali metals the range of applicability is extended up to the UV region, for the noble metals it is limited by the interband transitions occurring at optical frequencies.

Within the Drude model, when an EM radiation impinges on a metal, it causes the oscillatory movement of the electrons, which is damped only by the collisions of the free electrons against the positive core ions. The collision rate is determined by the *relaxation time* τ of the free electron gas, giving a characteristic frequency $\gamma = \tau^{-1}$ of the order of $10 - 100THz$ at room temperature.

The equation of motion for an electron of the gas under the effect of an external field $\mathbf{E}$ can be thus written:

$$m\ddot{\mathbf{x}} + m\gamma\dot{\mathbf{x}} = -e\mathbf{E}. \tag{1.10}$$

Assuming an oscillatory harmonic time dependence of the external electric field $\mathbf{E}(t) = \mathbf{E}_0 \mathrm{e}^{-i\omega t}$, leads to the solution for the displacement $\mathbf{x}$ of the electrons:

$$\mathbf{x}(t) = \frac{e}{m\left(\omega^2 + i\gamma\omega\right)}\mathbf{E}(t). \tag{1.11}$$

Considering that the overall polarization is given by $\mathbf{P} = -ne\mathbf{x}$ and remembering the relation $\mathbf{D} = \varepsilon_0\mathbf{E} + \mathbf{P}$, it follows:

$$\mathbf{P} = -\frac{ne^2}{m\left(\omega^2 + i\gamma\omega\right)}\mathbf{E} \tag{1.12a}$$

$$\mathbf{D} = \varepsilon_0\left(1 - \frac{\omega_\mathrm{p}^2}{\omega^2 + i\gamma\omega}\right)\mathbf{E} \tag{1.12b}$$

where was defined the *plasma frequency* of the free electron gas:

$$\omega_\mathrm{p}^2 = \frac{ne^2}{\varepsilon_0 m}. \tag{1.13}$$

As results, the complex dielectric function is obtained, and both real and imaginary part can be easily written:

$$\varepsilon(\omega) = \varepsilon_\infty - \frac{\omega_p^2}{\omega^2 + i\gamma\omega} = \left(\varepsilon_\infty - \frac{\omega_p^2}{\omega^2 + \gamma^2}\right) + i\left(\frac{\omega_p^2\gamma}{\omega\left(\omega^2 + \gamma^2\right)}\right) = \varepsilon_1(\omega) + i\varepsilon_2(\omega). \tag{1.14}$$

The parameter ε_∞ (usually between 1 and 10) takes into account the presence of a high polarization caused by d electrons near the Fermi surface, as for frequencies $\omega \gg \omega_p$, $\varepsilon(\omega) \to \varepsilon_\infty$ and $\mathbf{P}_\infty = \varepsilon_0\left(\varepsilon_\infty - 1\right)\mathbf{E}$.

Taking as reference what obtained from Johnson and Christy (Figure 1.1), the model reliability can be studied for different metals, and what emerges is a good agreement up to $600nm$ wavelength for copper and gold and up to $300nm$ for silver.

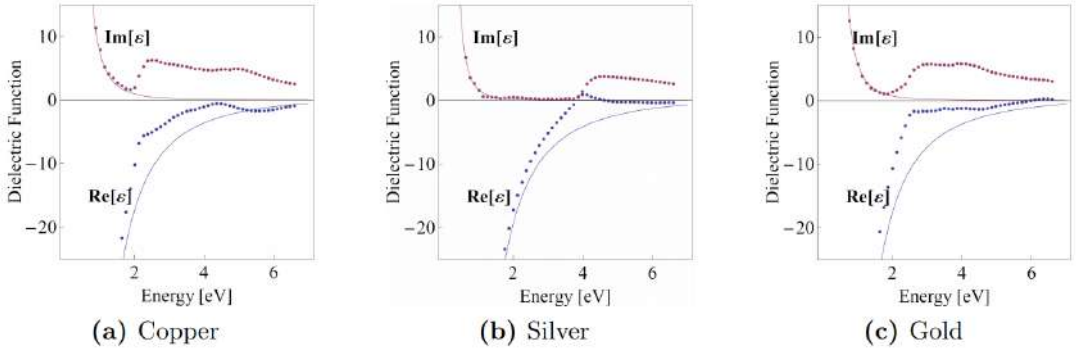

(a) Copper (b) Silver (c) Gold

Figure 1.1: Comparison between Drude model dielectric function (solid line) and experimental data from Johnson and Christy (dotted line) [2].

For frequencies $\omega < \omega_p$ the agreement of the Drude model with experimental data is quite good, at least up to the frequencies at which interband transitions became important.

1.1.2 Lorentz-Drude Model

An extension of the previous model allows to overcome the limit in frequency range due to the interband transitions. To take into account this effect, the *Lorentz-Drude model* adds in the motion equation (1.10) a harmonic term, that is the contribution of bounded electrons:

$$m\ddot{\mathbf{x}} + m\gamma\dot{\mathbf{x}} + m\omega_0^2\mathbf{x} = -e\mathbf{E} \tag{1.15}$$

where ω_0 is the resonance frequency associated to a specific transition of energy $\hbar\omega_0$. If many transitions are considered, the added term becomes a sum of oscillatory terms as the one added before, each one with its own resonance frequency ω_j and collision frequency γ_j.

Modelling the contribution of bounded electrons in this way, a corrected expression for the complex dielectric function can be obtained; in general, considering N different interband transitions, the dielectric function is corrected with respect to the Drude model one by the addition of N Lorentz-oscillator terms of resonance frequency ω_i and oscillatory strength S_i:

$$\varepsilon(\omega) = \varepsilon_\infty - \frac{\omega_p^2}{\omega^2 + i\gamma\omega} + \sum_{j=1}^{N} \frac{S_j}{\omega_j^2 - \omega^2 + i\gamma_j\omega}. \tag{1.16}$$

Again, a comparison between Johnson and Christy experimental data and Lorentz-Drude model dielectric function can be made in Figure 1.2, considering as theoretical trend the one obtained by Hao and Nordlander [3], starting from 4 Lorentzian interband transition terms.

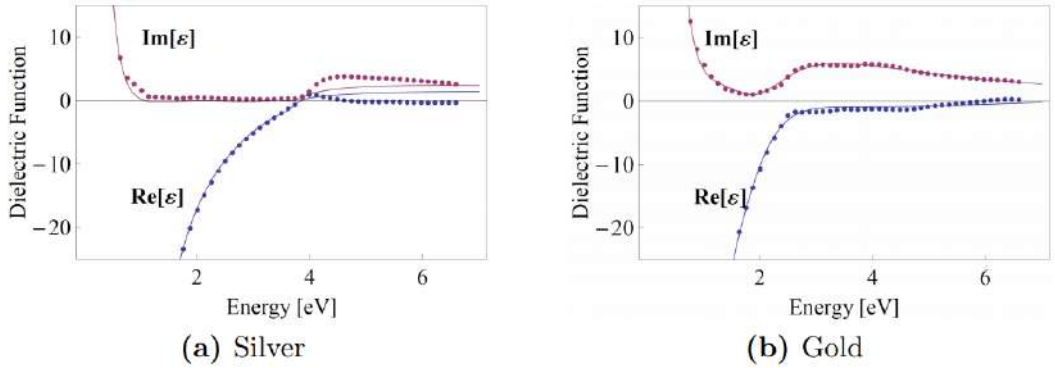

(a) Silver (b) Gold

Figure 1.2: Comparison between Drude-Lorentz model dielectric function (solid line) and experimental data from Johnson and Christy (dotted line) [2].

It is clear that the agreement is much better for the Lorentz-Drude model, in particular above the characteristic interband transition frequency for each metal.

1.2 Plasmon Polaritons Excitation

One of the most interesting phenomena arising from the interaction of EM waves with metallic nanostructures, under particular conditions, is the *plasmons oscillation*. *Plasmons* are, in general, collective resonant oscillations of the free electron gas of a metal. A preliminary distinction can distinguish between:

- *volume plasmon*, occurring in a bulk metal;
- *surface plasmon*, at the extended interface between metals and dielectrics;
- *localized surface plasmon* (LSP), at localized and spatially confined interface between metals and dielectrics.

1.2.1 Volume Plasmon

At sufficiently high frequencies metals become transparent to EM waves, supporting their propagation through them. This can be derived considering the dielectric function in the Drude model (equation (1.14)) when the condition $\omega > \omega_p \gg \gamma$ is fulfilled (interband transitions can be neglected too). In this assumption, dielectric function can be approximated with its real part only:

$$\varepsilon(\omega) \sim \varepsilon_1(\omega) = 1 - \frac{\omega_p^2}{\omega^2}. \tag{1.17}$$

It is possible to obtain the dispersion relation of the medium considering Maxwell's equations (1.1c) and (1.1d) (putting J_{ext} for our purposes) and approximating $\varepsilon(\omega)$ with equation (1.17). What derives is:

$$\nabla^2\mathbf{E} - \frac{\varepsilon}{c^2}\frac{\partial^2\mathbf{E}}{\partial t^2} = 0. \tag{1.18}$$

where important assumption are made over the dielectric function $\varepsilon(\mathbf{r}, t) = \varepsilon$, assuming both temporal independence and negligible variation of the dielectric profile over distances of the order of one optical wavelength.

If planar wave solution $\mathbf{E} = \mathbf{E}_0 e^{i(\mathbf{k}\cdot\mathbf{r}-\omega t)}$ is considered, the *dispersion relation* follows:

$$\omega^2 = \omega_p^2 + k^2c^2. \tag{1.19}$$

In the long wavelength limit ($|\mathbf{k}| \to 0$) the waves propagation is at a fixed *plasmon frequency* ω_p, which corresponds to a collective longitudinal oscillation of the gas of electrons inside positive ions lattice of the metal. A single quantum of this oscillation is called *volume plasmon*. Since volume plasmons are purely longitudinal oscillations, they cannot couple to EM radiation and the only way to get their excitation is through charged particles impact.

1.2.2 Surface Plasmon Polariton

As anticipated, *surface plasmon polaritons* (SPP) are excitations arising at the extended interface between metals and semiconductors. Differently from bulk volume plasmons, SPP are confined in a region spatially extending perpendicularly to the interface for sub-wavelength thicknesses where they propagates evanescently. Moreover, they result from the coupling of the EM fields with the electrons gas oscillations.

To characterize the SPP arising at the planar extended interface of metals and dielectrics, the discussion can start from the usual wave equation seen before (equation (1.18)), where the same assumptions are kept.

Again, a harmonic time dependence of the electric field $\mathbf{E} = \mathbf{E}_0 e^{i(\mathbf{k}\cdot\mathbf{r}-\omega t)}$ is assumed and, defining the wave vector of the propagating wave in vacuum $k_0 = \omega/c$, the *Helmoltz equation* is obtained:

$$\nabla^2\mathbf{E} + k_0^2\varepsilon\mathbf{E} = 0. \tag{1.20}$$

To simplify the problem, it is possible to choose a particular reference system and reduce a one-dimensional problem, schematically illustrated in Figure 1.3.

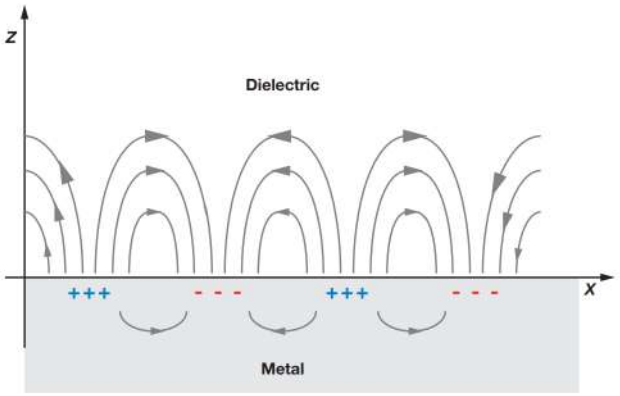

Figure 1.3: Schematic diagrams illustrating a surface plasmon polariton.

The waves propagation direction lays on the x axis and the spatial variation in the perpendicular y direction is null; thus the plane $z = 0$ is the one containing the metal-dielectric interface, where the oscillation propagates. The electric field can be simplified as $\mathbf{E}(x, y, z) = \mathbf{E}(z)\mathrm{e}^{i\beta x}$ where the complex parameter $\beta = k_x$ is the *propagation constant* of the waves, i.e., the wave vector component along the propagation direction.

These considerations lead to a simplified form of the Helmoltz equation (1.20):

$$\frac{\partial^2\mathbf{E}(z)}{\partial z^2} + \left(k_0^2\varepsilon - \beta^2\right)\mathbf{E} = 0. \tag{1.21}$$

Considering the corresponding relation obeyed by the magnetic field $\mathbf{H}$ and imposing proper boundary conditions at the interface for the fields (continuity of parallel or perpendicular components at the interface) a solution can be obtained.

However, it is intriguing to distinguish between transverse electric (TE) and transverse magnetic (TM) incident wave polarization. In fact it can be demonstrated that no surface plasmon polaritons modes exist for TE polarization, since they only exist for TM polarization, with the electric field solution propagating along x direction, having null component along y direction and evanescent component along z direction.

The dispersion relation of a SPP can be finally written as:

$$\beta = k_0\sqrt{\frac{\varepsilon\varepsilon_m}{\varepsilon + \varepsilon_m}} \tag{1.22}$$

where ε and ε_m are respectively the dielectric function of the metal and of the dielectric medium.

A more detailed analysis of the dispersion relation profile shows that for low frequencies (small wave vectors) the SPP propagation constant β keeps close to k_0 and waves extend over many wavelengths into the dielectric space. For high frequencies (large

wave vectors), on the other side, ω tends to the characteristic value of the *surface plasmon frequency* ω_{sp}:

$$\omega_{sp} = \frac{\omega_p}{\sqrt{1+\varepsilon_m}}. \tag{1.23}$$

As $\omega \to \omega_{sp}$, the mode, called *surface plasmon*, gain electrostatic character, with $\beta \to \infty$, implying the relation $\epsilon(\omega) + \epsilon_m = 0$, and $v_g \to 0$ (v_g group velocity of the oscillation).

A further consideration about SPP should be stressed, since even if their excitation is coupled to EM radiation, specific techniques for phase-matching are needed to effectively excite the modes. The reason of this property is that the propagation constant β is always greater than the wave vector k in the dielectric, making direct light incidence not sufficient to reach the excitation.

Most common employed techniques are *prism coupling* and *grating coupling*, in addition to highly focused beams or other different methods based on spatial mode-matching instead of phase-matching.

1.3 Localized Surface Plasmons

The last mode of excitation of the electrons sea in a metal at a dielectric interface, that will be entirely discussed in the present section, is the *Localized Surface Plasmon*. LSP excitation, as SPP, is coupled to electromagnetic field, but it is a localized, non-propagating mode deriving from absorption and scattering mechanisms of light impinging on a single nanoparticle, as shown in Figure 1.4, or in general, more complex three-dimensionally confined nanostructures.

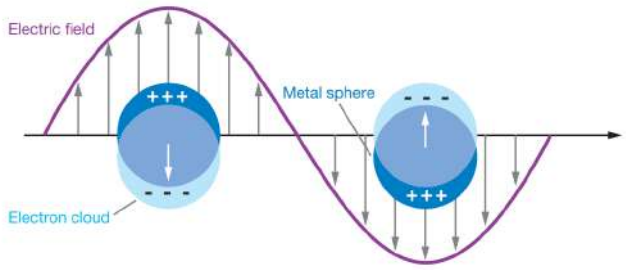

Figure 1.4: Schematic diagrams illustrating a localized surface plasmon.

When LSPs are excited, confined electrons are subjected to both the effect of the external exciting electric field and the internal restoring force that tends to keep the charge distribution in equilibrium; the result is the electrons motion of the form of a forced-damped harmonic oscillator. Moreover, if the light frequency matches the characteristic one of the metallic medium, that strongly depends on its shape, size and composition and on the dielectric constant of the embedding medium, the interaction results in the extremely important phenomenon called *localized surface plasmon resonance* (LSPR). At the resonance, the *local field enhancement* highly amplifies the total electric field, summed up by the external contribution and the *near-field* one, affected by the presence of the NP.

Finally, differently from SPP, LSP excitation does not require coupling methods to the incident radiation, since it directly arises from the light interaction.

1.3.1 Quasi-static Approximation for a Single Spherical Nanoparticle

As pointed out, LSP is an essentially simple resonant phenomenon arising from EM radiation interaction with nanostructures. Nevertheless, the characteristic properties, for example the spectral position of the resonant wavelength λ_{LSPR}, are in general complex function of many parameters, not analytically predictable. A powerful tool to solve problems of increasing complexity lies in computational simulations based on the resolution of partial differential equations through the Finite Element Method (FEM).

However, the problem of EM field interaction of a single perfectly spherical NP was widely developer by Gustav Mie in 1908.

The solid framework of the *Mie theory* will be now illustrated in the dipolar or quasi-static aproximation to treat this simple problem in the ideal case of a single non-interacting spherical particle with size much smaller than the EM wavelength.

The strongest assumption at the basis of the following reasoning is the *quasi-static approximation*, fulfilled if the characteristic dimension of the particle is much smaller than the incident light wavelength λ. The implication is that the harmonic electromagnetic oscillating field is almost constant in phase and spatially constant over the entire particle.

The system (Figure 1.5) consists in a homogeneous, isotropic sphere of radius a and dielectric constant $\varepsilon(\omega)$ embedded in a surrounding medium, isotropic and non-absorbing, of dielectric constant ε_m. The effect of a uniform, static electric field is added, with direction along the $\hat{z}$ direction $\mathbf{E} = E_0\hat{\mathbf{z}}$.

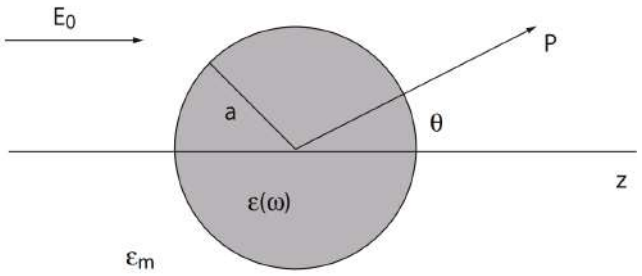

Figure 1.5: Sphere embedded in a dielectric medium and electric field.

The first aim is to solve the *Laplace equation* for the potential and derive the electric field solution:

$$\nabla^2\Phi = 0 \tag{1.24a}$$

$$\mathbf{E} = -\nabla\Phi. \tag{1.24b}$$

The solution of the problem is known, deriving from a multipolar expansion and from the spherical symmetry of the problem:

$$\Phi(r,\theta) = \sum_{l=0}^{\infty} \left[A_l \cdot r^l + B_l \cdot r^{-(l+1)}\right] P_l(\cos\theta) \tag{1.25}$$

with $P_l(\cos\theta)$ the Legendre Polynomials of order l, θ the angle between the position vector $\mathbf{r}$ at point P and the $\hat{z}$ direction. Imposing the finiteness of the electric potential at the origin and considering the boundary conditions both at infinity $r \longrightarrow \infty$ and at the sphere surface $r = a$, potentials inside and outside the sphere can be calculated.

An intuitive way of writing and consider the obtained solution is to model the particle as a dipole moment $\mathbf{p}$ induced by the external electric field and proportional to it in amplitude through the polarizability α:

$$\mathbf{p} = 4\pi\varepsilon_0\varepsilon_m a^3 \frac{\varepsilon - \varepsilon_m}{\varepsilon + 2\varepsilon_m}\mathbf{E}_0 \tag{1.26a}$$

$$\mathbf{p} = \varepsilon_0\varepsilon_m \alpha \mathbf{E}_0 \tag{1.26b}$$

$$\alpha = 4\pi a^3 \frac{\varepsilon - \varepsilon_m}{\varepsilon + 2\varepsilon_m}. \tag{1.26c}$$

The interesting clear consequence is that the polarizability α shows a resonance behaviour when the denominator $|\varepsilon + 2\varepsilon_m|$ of equation (1.26c) approaches zero. Due to the complex nature of ε and considering a negligible imaginary part $\mathrm{Im}[\varepsilon]$, the condition, called *Frölich condition*, reduces to:

$$\mathrm{Re}[\epsilon(\omega)] = -2\epsilon_m. \tag{1.27}$$

This oscillation mode of the metal nanoparticle is called *dipole surface plasmon*, and its characteristic frequency ω_{LSPR} is strongly linked to the dielectric constant of the embedding medium ε_m.

Moreover, the α resonance is strictly related to the *local field enhancement*, as Frölich condition implies the amplification of the electric fields inside and outside the NP:

$$\mathbf{E}_{\text{in}} = \frac{3\varepsilon_m}{\varepsilon + 2\varepsilon_m}\mathbf{E}_0 \tag{1.28a}$$

$$\mathbf{E}_{\text{out}} = \mathbf{E}_0 + \frac{3\mathbf{n}(\mathbf{n}\cdot\mathbf{p}) - \mathbf{p}}{4\pi\varepsilon_0\varepsilon_m}\frac{1}{r^3}, \tag{1.28b}$$

where $\mathbf{n}$ is the versor along the scattering direction.

1.3.2 Mie Theory

The Mie theory, in its quasi-static approximation, leads as shown to the fully description of the light interaction (absorption, scattering) with a small spherical nanoparticle and to the explanation of the LSPR phenomenon as resonant enhancement of the electric field and resonant amplification of the particle polarizability.

The validity of quasi-static approximation is still limited to small particles, with a good agreement only for particles with dimension well below $100nm$ interacting with radiation in the visible or near-infrared spectral region.

When particles dimensions overcome this threshold, the approximation cannot be reasonably held, since the electric field significantly vary in space over the particle volume, in terms of phase non-uniformity, requiring a more complex electrodynamic treatment. A rigorous and complete theory was developed by Mie to take into account this aspect, computing the scattered and absorbed radiation of a sphere, expanding both internal and external scattered fields in terms of normal harmonic modes. Since the detail of the theory are beyond the applications and aims of this work, the particulars of the theory are left and not showed.

One interesting result of Mie theory beyond the dipolar approximation is reported in the following without demonstration, giving the polarizability α of a larger spherical particle of radius a and volume V and dielectric function ε:

$$\alpha = \frac{1 - \left(\frac{1}{10}\right)(\varepsilon + \varepsilon_m)\, x^2 + O\left(x^4\right)}{\left(\frac{1}{3} + \frac{\varepsilon_m}{\varepsilon - \varepsilon_m}\right) - \frac{1}{30}(\varepsilon + 10\varepsilon_m)\, x^2 - i\frac{4\pi^2 \varepsilon_m^{3/2}}{3}\frac{V}{\lambda_0^3} + O\left(x^4\right)} V \tag{1.29}$$

with $x = \frac{\pi a}{\lambda_0}$ defined as *size parameter* of the particle, proportional to the ratio between the radius and the free-space wavelength λ_0 [1].

The correction with respect to the simpler approximated expression (1.26c) involving different powers of the size parameter, with the quadratic term at the numerator accounting for the retardation of the exciting field over the entire sphere volume, while the quadratic term at the denominator is linked to the retardation of the depolarization field inside the particle. Both these effects reflect in a redshift of the LSPR peak.

This latter term also includes an increase of polarization and decreasing influence of the absorption, with an effect balanced by the last imaginary term at the denominator, linked to the *radiation damping*. Higher order terms are not explicitly included, standing for higher order resonances.

The overall effect of bigger dimensions beyond the quasi-static approximation limit is the result of two opposite processes: a radiative decay process into photons, dominating for larger particles, and a non-radiative process related to absorption.

Considering even smaller particles, with a radius of the order or less than $10nm$ or down to $1nm$, more complex effect must be considered, as *chemical interface damping* or the beginning of quantum effects.

1.3.3 LSPR in Particle Ensembles and Hot-Spots

The simple problem exactly solvable of a single spherical nanoparticle interacting with EM fields is far from the real usual applications where ensemble of nanoparticles or, more often, nanostructured geometries are realized and employed. In those cases, LSPR excitation is clearly influenced and determined by the electromagnetic interactions between the localized modes [4].

For example, a system of ordered metal nanoparticle arrays can be studied. Considering many particles of size a arranged in one- or two-dimensional arrays with interparticle spacing d, the assumption $a \ll d$ is made, in order to allow dipolar approximation and treat the particles as point dipoles.

The interspacing parameter d plays an important role, distinguish between different regimes. If $d \ll \lambda$, particles are closely spaced and near-field interactions with a distance dependence of d^{-3} dominate. This leads to the presence of strong field localization at the nano-sized gaps between particles, thanks to a suppression of scattering into the far-field. Such regions of high field enhancement are the so called *hot-spots* of extremely high importance and wide range of applications.

For larger particle separation $d \gg \lambda$, finally, far-field dipolar coupling dominates with a distance dependence of d^{-1}.

Chapter 2

LSPR-Based Plasmonic Biosensors

To give an intuitive idea of what a *biosensor* is and how it works, it can be briefly defined as a device that uses biological or chemical receptors to detect the presence of analytes (molecules) in a sample and, more in general, to give detailed information on the binding affinity and kinetics of the interaction of interest. The detection event is transduced as a measurable and quantifiable signal, for example electrical or optical signal [5].

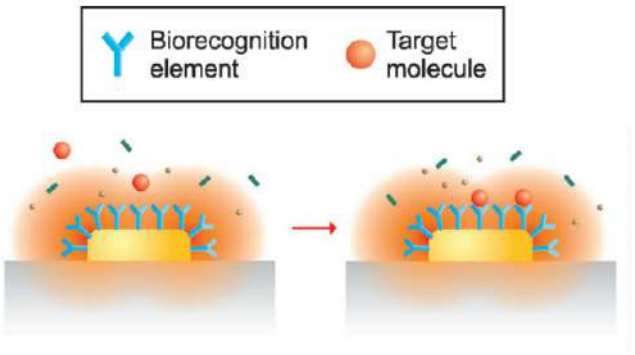

Figure 2.1: Schematical representation of an affinity biosensor [6].

The link between plasmonics and molecular biosensing and the brilliant finding that the potential of nano-scale light-matter interaction phenomena can be applied in this field, came out only between 1970s and 1980s. When Fleischmann *et al.* [7] observed an unexpected enhancement of Raman scattering near a roughened metal surface, researches on nanophotonic mechanisms spread out and revealed that the phenomenon was to be attributed to the excitations of EM modes of the metals. Since then, both theoretical investigations and experimental applications highly increased, until Liedberg *et al.* [8] realized the very first plasmonic nanobiosensor, exploiting SPR of a metal film to detect the adsorption of molecules onto its surface via refractive index (RI) change.

Over the last decades, along with the fast development in nanofabrication techniques, SPR biosensing has made great advance and their application has been boosted in wide research and industry areas. Examples to mention are food safety with the detection of foodborne pathogen [9], drug discovery and delivery [10], environment

monitoring [11], presence of heavy ions in water, and medical diagnostics [12].

In particular, the detection and quantification of disease-associated biomolecules, such as proteins and nucleic acids, in tissues and biological fluids are crucial for accurate diagnoses and reliable prognoses and thus requires optimal detection strategies. Today, although different consolidated methods are present, as enzyme-linked immunosorbent assays (ELISAs), western blot or the well known polymerase chain reaction (PCR), they all show limitations that need to be overcome, and LSPR biosensors are powerful promising candidates for this purpose. Weaknesses are in particular related to the labeling process required to promote the selective binding of the biomolecule of interest, or the expensive and time-consuming amplification process, needful for techniques as PCR to enhance the response in low concentration samples.

LSPR biosensors instead are *label-free* sensors and thus do not require any use of reporter elements (fluorescent, luminescent, radiometric, or colorimetric), thus providing information beyond the presence/absence of a target molecule, also about the binding reaction and kinetics. Moreover, the advantages of LSPR-based nanobiosensors rely upon their high sensitivity and spatial resolution, the real-time assay accessibility using microfluidic systems, low cost and easy instrumental setup.

Nevertheless significant challenges remain in the world of plasmonic biosensors, starting from sensitivity and limit of detection, with good chances to be pushed even towards the single-molecule detection limit [13], selectivity in complex biological solutions like blood and urine, compatibility with membrane proteins and point of care (POC) diagnostic devices, the possibility of in vivo experiments [14] or combining with molecular identification techniques and the practical development of proper instrumentation for routine and high-throughput detection.

In this chapter the fundamentals of the theory behind a LSPR nanobiosensor will be illustrated, along with the evaluation of a biosensor performance characteristics; next attention will be focused on the optical platforms configuration employed in biosensing experiment and, finally, on the basics of functionalization techniques and issues.

2.1 Refractive Index Sensing

LSPR biosensors, and more in general SPR biosensors, are refractive index-based biosensors, meaning that their working principle (illustrated in Figure 2.2) is based upon their sensitivity to changes in the medium surrounding their surfaces [15].

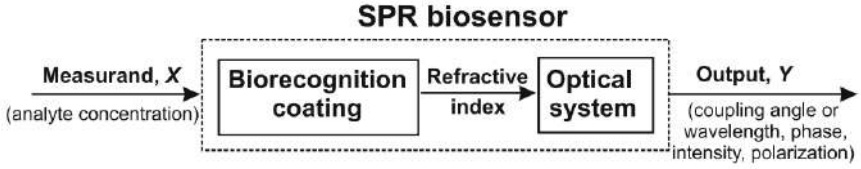

Figure 2.2: Refractive index biosensors working principle.

The surrounding medium RI dependence can be easily seen looking at the expression (1.22) for the propagating constant β of the surface plasmon at metal-dielectric interface

$$\beta = k_0 \sqrt{\frac{\varepsilon \varepsilon_m}{\varepsilon + \varepsilon_m}} \tag{2.1}$$

remembering that the refractive index of the medium n_m is related to its dielectric function ε_m through $n_m = \sqrt{\varepsilon_m}$.

More in detail, for a LSPR biosensors, the change in refractive index of the medium in which the sensor itself is embedded, is the input signal that is detected and transduced in output as a wavelength shift in the resonance extinction (or scattering) peak λ_{LSPR}.

The trend is a linear proportionality, with an exact relationship found by Van Duyne [16], [17] in case of a sensor embedded in an environment with refractive index n_{env} with an adsorbate of effective thickness t and refractive index n_s is put at the interface between the sensor and the surrounding medium. What was found is the following linear relationship

$$\Delta\lambda_{LSPR} = m\Delta n\,[1 - \exp\,(-2t/l_d)] \tag{2.2}$$

where m is the bulk sensitivity of the sensor, $\Delta n = n_s - n_{env}$ and l_d is the characteristic EM-field-decay length (approximated as an exponential decay). This relationship is the basis of LSPR wavelength-shift sensing experiments, the most common method for LSPR sensing in which the change in the maximum (or minimum) of the LSPR extinction curve is monitored as a function of changes in the local dielectric environment caused by analyte adsorption.

2.1.1 Substrate Size and Shape Dependence

Since the extinction (scattering) spectra of a nanostructure intrinsically depends on parameters like characteristic dimension, shape, aspect ratio, composition [18] (as can be clearly seen in Figure 2.3), what follows is that the performances of a nanostructure employed as LSPR biosensor are strictly related to its structural properties. For this reason, a rational material design is crucial for sensing applications.

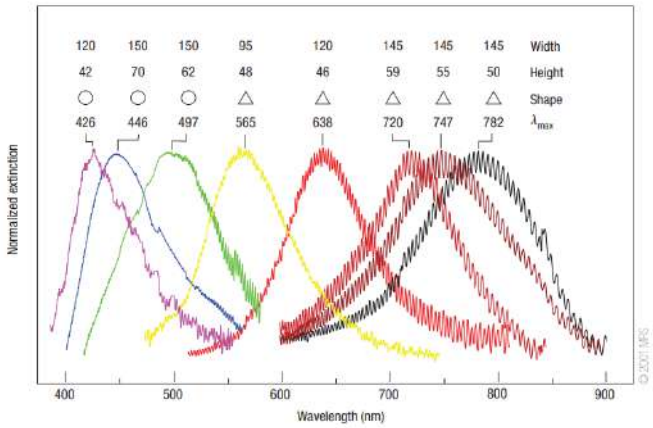

Figure 2.3: Effect of size and shape on LSPR extinction spectrum for silver nanoprisms and nanodiscs [18].

For example, testing nanoparticles with various shape and morphology under condition of same refractive index of the embedding solvent, shows that spherical, triangular, rod-like NPs exhibited different sensitivity. In general, what derives is that increasing the aspect ratio (width/height) of NPs results in redshifts in λ_{LSPR}, higher bulk sensitivity values and longer electromagnetic field decay lengths l_d [18].

In addition, the effective electromagnetic decay length l_d can be tuned by changing the thickness and lateral dimensions of arrays of three-dimensional nanostructures, considering the short-range and long-range distance dependence of the field [19], [20].

Finally, theoretical modelling has shown that sharp nanoparticle features give rise to more intense hot-spots in the electromagnetic fields that increase the sensitivity to local refractive index [21], [22].

2.1.2 Performance Characteristics

To quantitatively evaluate the sensing performances of a plasmonic biosensor, the main parameters, related to the ability of a sensor to detect an analyte present in solution, are essentially three: *sensitivity*, *resolution* and *limit of detection* [23].

The *sensitivity* S of a plasmonic sensor is the ratio of the change in sensor output Y to the change in the quantity to be measured, that is the refractive index n_s at the sensor surface. It corresponds to the amount of change in sensor output response resulting from a unitary change in RI. This parameter is more accurately referred to as the sensor *bulk sensitivity* S_∞:

$$S_\infty = \frac{\partial Y}{\partial n_s}. \tag{2.3}$$

A slightly different definition is the one for the *local sensitivity* S_0. This parameter, also called *surface sensibility*, is defined as the second derivative of the sensor output Y with respect to the refractive index n_s variation and to the thickness t of a dielectric layer of refractive index n_s that is added on the surface, for $t \to 0$:

$$S_0 = \left.\frac{\partial^2 Y}{\partial n_s \partial t}\right|_{t=0} \cong \frac{1}{\Delta n_s} \cdot \left.\frac{\partial Y}{\partial t}\right|_{t=0}. \tag{2.4}$$

Where the bulk sensitivity accounts for the sensor output if the whole environment around changes, the local sensitivity takes into account the effect of refractive index change at the sensor interface, inside a thin layer of fixed thickness.

A further significant parameter is the *resolution* σ. The resolution of a biosensor defines the smallest change in the refractive index that produces a detectable change in the sensor output. Notably, the minimum sensor output change that can be detected depends on the level of uncertainty of the sensor output, the output noise. It is typically expressed in terms of the standard deviation of noise of the sensor output σ_{SO} and bulk sensitivity S_∞:

$$\sigma = \frac{\sigma_{\mathrm{SO}}}{S_\infty}. \tag{2.5}$$

The last characteristic parameter of a plasmonic biosensor is its *limit of detection* (LOD). The LOD optimally describes the bioanalytical power of a biosensor, representing the smallest concentration (or amount) of analyte that can be reliably detected by a specific measurement process. It is usually defined as the concentration of analyte that produces a sensor response corresponding to three standard deviations of the sensor response measured for a blank sample σ_b (sample with no analyte):

$$\mathrm{LOD} = \frac{3\sigma_b}{S_C} \tag{2.6}$$

where S_c is the change in the sensor output divided by the change in the concentration of analyte producing it.

Considering the wavelength-shift based LSPR biosensors, for which the relation (2.2) holds, analytical expression for S_∞, S_0 and their reciprocal relationship can be deduced:

$$S_0 = \left.\frac{\partial^2 \lambda\,(t, n_s)}{\partial n_s \partial t}\right|_{t=0} = \frac{2m}{l_d} \tag{2.7a}$$

$$S_\infty = \lim_{t\to\infty}\left(\frac{\partial \lambda\,(t, n_s)}{\partial n_s}\right) = m \tag{2.7b}$$

$$S_0 = \frac{2 \cdot S_\infty}{l_d}. \tag{2.7c}$$

2.2 Instrumental Optical Setup for LSPR Sensing

Performances of a plasmonic biosensors are deeply related not only to the biosensor itself, meaning on the design and material engineering of the nanostructure employed as sensing substrate, but also to the experimental hardware setup [24]. The optical platform, indeed, has a direct impact on the biosensor performance characteristics, such as resolution or limit of detection.

Since plasmonic biosensors activity consists in proper excitation of EM modes, the coupling with an EM fields source is of primary importance. In general, SPR nanobiosensors, whose working principle is the excitation of surface plasmons, require a complex coupling system allowing the excitation of modes that cannot be achieved with a simple and not controlled light-matter interaction. One of the most common method to couple EM incident radiation with SPR sensors is for example the optical configuration of *prism coupling*, with output signal analysis based on an interrogation method based on wavelength, intensity or phase analysis [25].

LSPR biosensors, on the contrary, show the clear advantage of being independent on complex coupling method and directly excitable via incident light interaction. Instrumental setup for LSPR biosensing experiment is usually build up by an illumination source that can range from a highly stabilized laser to an inexpensive LED or halogen bulb, in addition to an instrument gathering the information about light reflected from or transmitted through the sensor [26].

Among several approaches to the measurements of LSPR spectra, the most straightforward is transmission UV-Vis spectroscopy, where the extinction spectrum (i.e. absorption and scattering) of the nanoparticles is acquired by recording the wavelength dependence of the light passing through the sample.

Nevertheless, more complex optical configurations exist. For non-transparent samples, for example, reflective geometry are needful and, in these cases, the sensor output response is recorded as the minimum of the reflection extinction curve. Even more advanced applications, for example, rely upon extremely powerful techniques of dark-field scattering microscopy measurements (see Figure 2.4 [27]).

2.2.1 Microfluidic Systems

A practical implementation of LSPR sensors has to meet some practical issues, deriving for example from the requirement of low noise, fast and real-time response, low sample consumption. This latter point, in particular, significantly came out in case of low or limited concentrations of analyte in the sample, when an appropriate system for the efficient delivery of analyte to active regions of the sensor surface is necessary in order to reach unambiguous response in a short time.

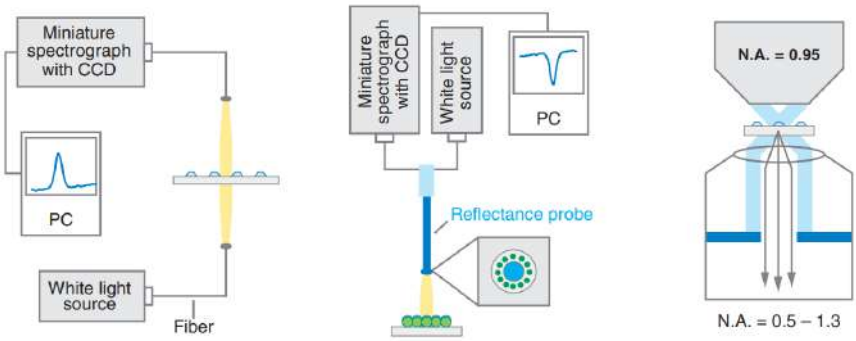

Figure 2.4: Examples of measuring experimental setup; from left to right, transmission, reflectance spectroscopy geometry and dark-field microscopy setup [27].

The solution to this question usually finds an optimal solution in properly designed microfluidic devices. In the last few years, a large amount of work has been directed toward the use of microfluidic systems to improve both the efficiency of analyte delivery and the sensor throughput, in addition to allow sample manipulation optimization and ease of use.

Most common biosensing microfluidic systems are single channel microfluidic chip (Figure 2.5), of crucial importance for testing the sensing properties of a given plasmonic structure [6].

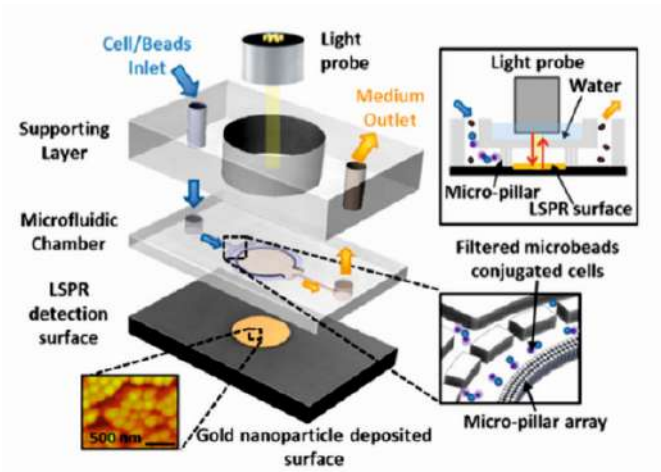

Figure 2.5: Example of integrated system for selective delivery of molecules to sensing area [6].

Progress and development of both biosensing nanostructures and microfluidic realizations led to a need of multichannel microfluidic chip, allowing throughput increasing and precise delivery of liquid samples to multiple detection spots.

During the last few years there has been a large effort directed toward the development of multichannel integrated microfluidic chips for sensors based on plasmonic nanostructures; in the current literature such systems can be found to have up to several tens of independent channels [28], [29].

2.3 Functionalization Protocols

In the last years, a big effort was made in order to push even further the quality of plasmonic nanobiosensors performances, i.e., their sensitivity, resolution and LOD. To pursue this aim, challenges are related to the nanostructure design and detection setup, as well as to functionalization methods. The demand for methods enabling the functionalization with new and different biomolecules (antibodies, enzymes, peptides, nucleic acids, or aptamers) is expanding, since the biosensor receptors recognize and capture the target molecule, referred to as analyte, onto its surface.

For this reason, the sensor selectivity, its affinity with the analyte and the immobilization of this latter one, are of outmost importance for proper functioning and performances of the sensor.

Essential prerequisites of an ideal functionalization protocol are its ability to provide the desired receptors concentration, to preserve the biological activity of both receptors and analyte, to suppress the nonspecific adsorption to the active area of the sensor. In addition, all the listed issues are tangled up by the challenges in the molecules immobilization onto nanostructured non planar biosensors surfaces, often exhibiting more or less pronounced curvatures or ensemble of different materials. Moreover, in biosensors based on plasmonic nanostructures, it is desirable that the receptors are not attached to the entire metal surface, but rather to the active areas (hot spots), where the EM field is strongly enhanced, requiring special functionalization strategies that enable spatial resolution [30], [31].

Finally, the rational design of a functionalization method and the binding mechanism at its basis have to match the demand for being controlled and providing a temporal profile of the sensor response (as in the case of example in Figure 2.6). This translates to the rigorous determination of binding kinetics and provides important information about interacting molecules, allowing to build an appropriate kinetic model of molecular interaction to completely describe the LSPR biosensor response and binding reaction.

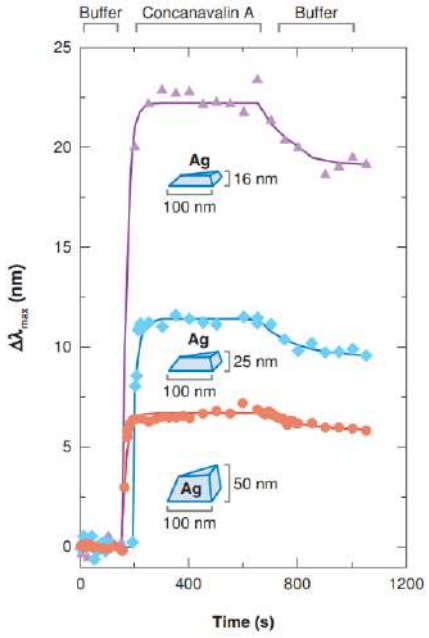

Figure 2.6: Real time kinetic response of mannose-functionalized Ag nanosensor of different heights on exposure to concanavalin A followed by washing with buffer [27].

Chapter 3

Nanofabrication of Plasmoinc Nanoprism Arrays

As previously mentioned, the performances of a plasmonic biosensor strongly depend on the sample morphology, geometry and characteristic dimensions. For this reason it is worth to stress the importance of designing and fabricating the biosensing nanostructures. The ideal nanofabrication technique should ensure a fine tunability and steady control of the involved parameter with good sensitivity and reproducibility. At the same time, high throughput and cost-effectiveness of the synthesis method play an important role in the choice of the nanofabrication technique.

The highest throughput methods employed in the production of ordered 2D arrays of plasmonic nanostructures for different applications, as well as more complicated nanopattern, are all based on the *lithography* technique. Lithography refers to the fabrication of nanostructures replicating patterns into underlying substrates with the help of a proper mask or in a maskless way. Common lithographic techniques are for example *electron beam lithography*, *focused ion beam lithography*, *photolithography*, *colloidal lithography* or *nanoimprinting lithography*.

The powerful nanofabrication technique employed in this work for the synthesis of the ordered 2D nanoprism arrays (NPAs) is a bottom-up, cost-effective and high-throughput technique called *Nanosphere Lithography* (NSL). All the steps of the method will be in-deep described in the following sections, then the detail about the post-treatment processes of the sample will follow.

3.1 Nanosphere Lithography

Nanosphere lithography is a technique used to generate planar extended layers of hexagonally close packed nanostructures [32], [33]. The strengths of this method lay in the capability to provide regularity and homogeneity in relatively wide ($\sim cm^2$) arrays of nanoparticles for different sizes and with precisely controlled spacings. In addition, it is relatively not expensive and easy to be implemented.

The technique is based on the self-assembly of nanoscale objects to create a periodic pattern or mask. In particular, a solution of size-monodispersed polymeric nanospheres is delivered to a flat substrate, where the self-assembly into hexagonal close-packed structure and the solvent evaporation leads to the presence of voids between nanospheres, where the initial substrate is exposed.

The ordered layer, referred to as *mask*, is used to pattern the underlying substrate, typically via metal deposition. Finally, the mask removal leaves an ordered pattern of

pyramids, or *nanoprisms* in the regions corresponding to the void spaces between the nanospheres.

The steps of the process are depicted in the following Figure.

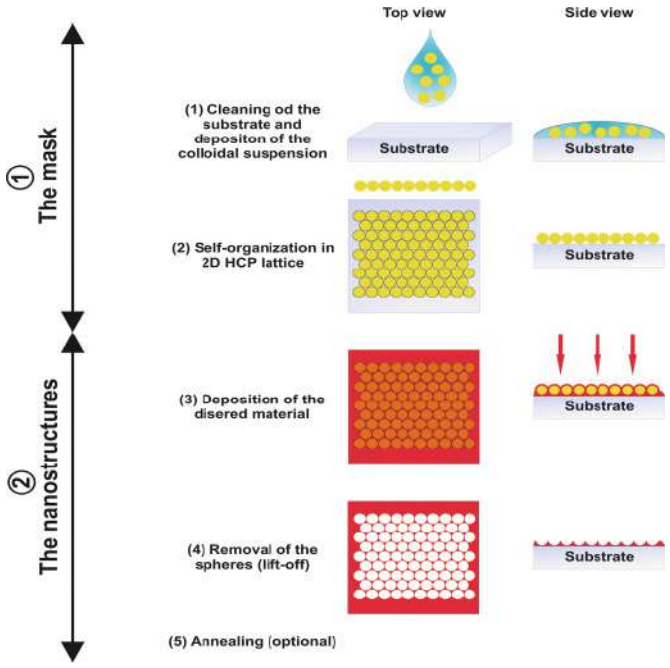

Figure 3.1: Illustration of NSL nanofabrication process steps [34].

Each of the described phases will be further described in the next paragraphs, starting from the substrate preparation and mask fabrication, up to the consecutive metal deposition and postprocessing.

3.1.1 Substrate Preparation

The substrate over which the metallic NPAs nanostructure is nanofabricated is a square slide (lateral size of $2cm$ and thickness of $1mm$ approximately) of silica (SiO_2). The initial necessary step in the fabrication process is the cleaning of the substrates.

This operation is needful in order to remove any kind of impurities on the substrate surface, such as dust or organic residuals, thus avoiding the formation of defects during the mask assembling and drying, as line defects, vacancies, dislocations or polycrystalline domains.

The cleaning process consists in two controlled baths and proper rinsing in between.

First an *acid piranha* is performed. The piranha solution is a mixture of sulfuric acid (H_2SO_4) and hydrogen peroxide (H_2O_2) in 3:1 ratio. The substrates are immersed in a becher containing about $120mL$ of the piranha solution and placed over a hot plate at fixed temperature of 90 °C for about 1 hour. The acid bath removes the surface impurities (mostly organic ones) and is crucial to promote a high level of hydrophilicity of the substrate.

When the process is completed, the substrates are throughly flushed using Milli-Q water (highly purified and deionized, $18.2M\Omega \cdot cm$ resistivity), with three consecutive rinsing in approximately $200mL$ of water.

The substrates are then immersed in a *basic piranha* solution of ammonium hydroxide (NH_4OH) and hydrogen peroxide in the same 3:1 ratio. Again the bath is

controlled at a temperature of 90 °C for about half an hour. Finally an intense rinsing is made with the same procedure employed after the acid piranha.

After the basic bath the cleaning process is completed, and the highly hydrophilic, without impurities, substrates are stored immersed in Milli-Q water, ready to be decored with the mask.

3.1.2 Polystyrene Nanosphere Mask

To obtain the self-assembled layer of hexagonal close-packed nanospheres, a solution of polysterene nanoparticles is used. The NPs are monodispersed in size, with a nominal diameter of the spheres of $522nm$. The choice of this dimension is supported by experimental trial which demonstrated that $522nm$ diameter polystyrene NPs, instead of $314nm$ ones for example, allow to form quite extended masks (areas of the order of cm^2) with few line or point defects and homogeneity in terms of polycrystalline domains.

The nanospheres solution is first diluted in 50:50 ratio with isopropyl alcohol (2-propanol); then it is sonicated in ultrasonic bath for 5 minutes, centrifugated for 5 minutes at $12rpm$ velocity and decanted to separate the solvent and the sedimented NP. These ones are refilled with a solution of Milli-Q water and 2-propanol (50:50) and the entire procedure is repeated for three times. At this point the colloidal suspension of nanospheres can be used.

Since both the self-assembling of the mask and the drying process are strictly influenced and eventually compromised by the thermodynamic external conditions, the next steps have to take place inside a semi-isolated chamber with controlled and tunable temperature and humidity. In particular, the best working conditions are obtained with temperature and humidity values of about 27 °C and 80 %, respectively.

The system inside the chamber is composed of a crystallizer filled with Milli-Q water at temperature of 30 °C approximately; the crystallizer is placed over a slab that isolates it from the movements and ensure stability.

A motorized dipper is provided with a movable T-shaped arm whose ascent and descent velocity can be tuned. A cleaned substrate is fixed on the movable arm in order to be dipped in or extracted from the warm water.

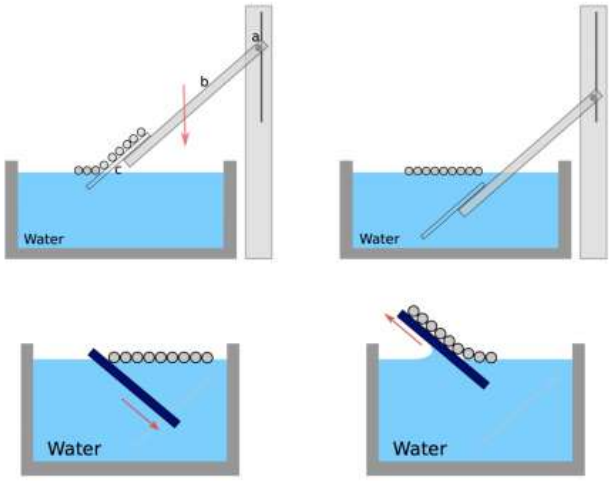

Figure 3.2: Representation of the motorized dipper and of the slide descent and ascent stage.

At this point the substrate is uniformly coated with $25\mu L$ of the colloidal solution and completely dipped into water. This descent stage is performed at a proper velocity, avoiding too fast movement and immersion which lead to turbulent diffusion of the solution in water, as well as too slow descent that causes the rapid evaporation of the solvent and presence of defects in the mask. The NPs floating on the water surface assemble in a compact monolayer on the surface of water, thanks to the alcohol evaporation.

The mask has to be collected on the surface of a new substrate, where the adhesion is favored by the high hydrophilicity and the environment conditions. This step is not automated and is completely manual, since the substrate, held by tweezers, is dipped into water by hand. Extremely steady and controlled movement allow the mask to adhere on the substrate and to pull the slide out of water (see Figure 3.2).

Hence, the substrate covered by the mask is positioned vertically and left inside the chamber where the drying process takes place, gradually bringing back temperature and humidity values to the room ones. This ensure a proper evaporation speed of the solvent from the NPs mask, reflected in a defectless mask.

The final look of the substrates covered by masks is shown in Figure 3.3, and can be seen as an irridescent area with high uniformity.

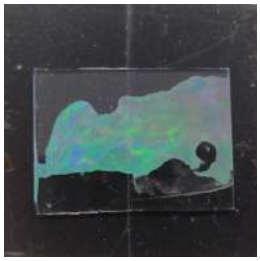

Figure 3.3: PS self-assembled mask, visible as a macroscopic iridescent region covering the silica slide ($2cmx1cm$).

On the nanoscale, the honeycomb structure of triangular nanoprisms will be geometrically characterized by the PS nanosphere diameter D, as can be seen in Figure 3.4. It can be shown in fact that the distance between neighbour prisms will be equal to the interstitial distance of the PS nanospheres pattern, that is

$$d = \frac{D}{\sqrt{3}} \approx 301nm \tag{3.1}$$

and the lateral in-plane dimension of the triangular base a is linked to the diameter D through the relationship

$$a = \frac{3}{2}\left(\sqrt{3} - 1 - \frac{1}{\sqrt{3}}\right) D \approx 0.233D \approx 122nm. \tag{3.2}$$

3.1.3 Thermal Evaporation Deposition

The last step for the NPAs production is the metal deposition via thermal evaporation. In this work the deposition is performed consecutively for a thin layer of chromium ($2nm$ nominal thickness), which acts as an adhesive layer between the substrate and the metal, and a thicker layer of gold (about $70nm$ nominal thickness). Moreover, the deposition is not performed covering the entire substrate surface, instead a phosphorous bronze mask with 4 holes with $2mm$ diameter is placed over the substrate, thus

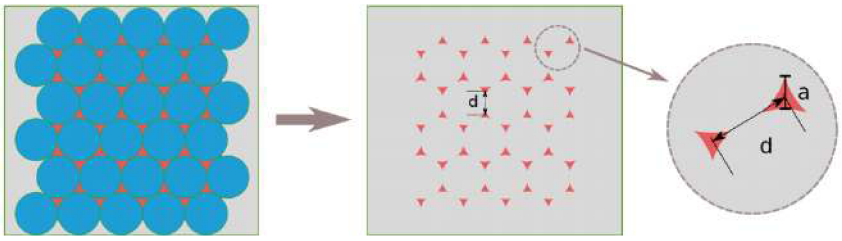

Figure 3.4: NPAs obtained with NSL and characteristic dimensions.

depositing the film just on these spots for reasons of convenience during the measurements.

Thermal evaporation technique consists in the deposition of a thin layer of a material, referred to as target, placed in a crucible made of a metal with high melting temperature. When sufficiently high current (tunable) flows through the crucible, the heat generated by Joule effect is transferred to the target, promoting its evaporation. Everything is placed inside an isolated chamber where the pression is controlled and vacuum pumps are connected to reach the desired level. The operation is indeed carried out in vacuum condition ($10^{-5} mbar$), to avoid contaminations or metal oxidation reactions.

A schematic representation of the entire experimental apparatus is shown in Figure 3.5.

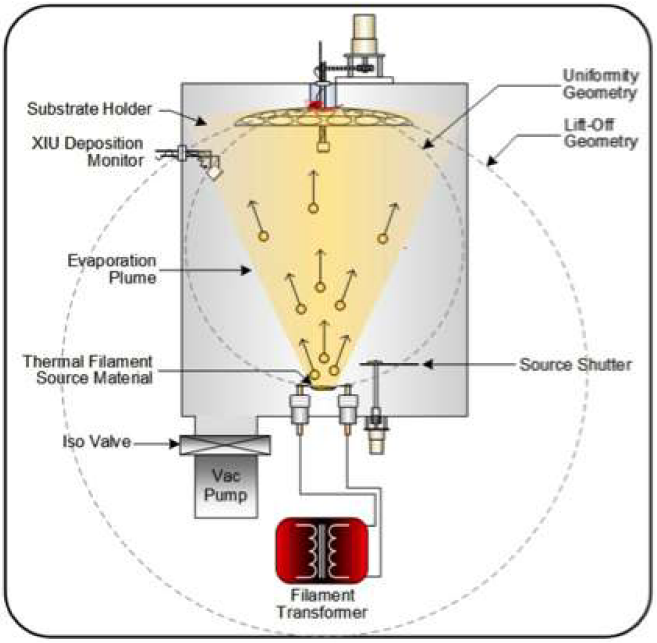

Figure 3.5: Schematical representation of the thermal evaporation setup.

When the evaporated atoms of the metal reach the sample, they condensate and form the film.

In addition, a Quartz Crystal Microbalance is connected to the sample holder and allow to control the deposition process in terms of mass deposition velocity and total deposited mass. A calibration of the system is performed to convert this data in the correspondent film height and to stop the process once the desired value is obtained.

A shutter is mounted between the target and the sample holder, with the possibility to instantly isolate this latter one from the evaporated metal atoms that would be deposited as well on the sample and overcome the wanted mass threshold.

In the present work, as mentioned, two consecutive evaporation of different metals (Cr, Au) are performed; the chamber is equipped with a crucible for each of the metals, in particular a crucible made of tungsten for gold target and a crucible made of tantalium for chromium. The difference is due to the different evaporation temperatures of the target metals and to the Au disposition to form low-melting alloy with tantalum.

The technical parameters of the thermal evaporation deposition performed in the present work are shown in the following Table:

	Pressure (mbar)	Current (A)	Rate (Å/s)
Cr	10^{-6}	90	0.2
Au	10^{-5}	160	7

Table 3.1: Values of pression, current and rate for thermal evaporation used in the present work.

Samples labeling is made with the number of the evaporation process preceded by the letter E, standing for evaporation, and eventually followed by the number of the spot employed for the sensing experiment (for example E488B-02 is the name associated to the second spot of the sample fabricated with the thermal evaporation process number 488.).

SEM images of the fabricated sample were acquired as shown in Figure 3.6. The nanostructure morphology is of optimal quality, with nanotriangles well defined in shape and with quite extended defectless areas.

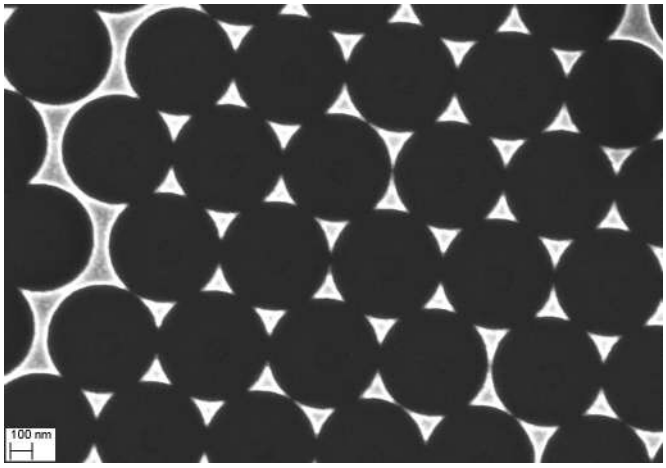

Figure 3.6: SEM image of NanoPrisms Array obtained by NSL with polystyrene nanospheres of $522nm$ diameter.

3.2 Sample Post-treatment

The substrates thus produced, after the thermal evaporation, need to be cleaned from the polystyrene NPs still covering the active areas. The nanospheres removal is first performed by simply peeling them off with adhesive tape and then consecutively rinsing the substrates in toluene, acetone and ethanol. Drying the samples with

compressed air flow makes it in principle ready to be used.

Nevertheless, as can be seen from SEM images in Figure 3.7, the obtained nanotriangles are well defined but show a halo of nanoparticles. These residuals are a side effect of the employed nanofabrication technique, since the deposition of the evaporated atoms is able to strike the small interstices between a nanosphere and the underlying silica substrate, producing these nano-agglomerates called *nanosatellites*.

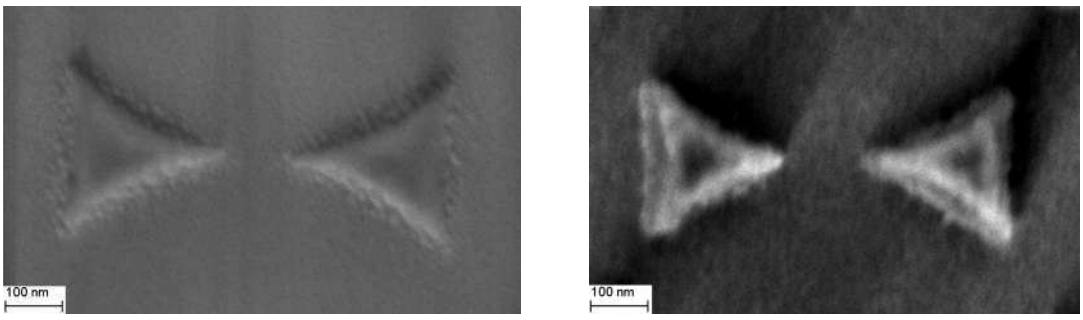

(a) (b)

Figure 3.7: Zoomed SEM images of NPA before (a) and after (b) the post-treatment process. Nanosatellites byproducts are clearly visible covering the substrate surface near the nanotriangles, while they are successfully removed after the physical post-treatment treatment which moreover preserves the pyramids tips and edge.

The presence of this byproduct directly determine the performances of the substrate as LSPR biosensors, resulting in a characteristic resonance absorbance peak of low quality, broadened and not sharp as desirable. For this reason, nanosatellites need to be removed, and a post-treatment process needs to be applied to accomplish this task.

Two possible solutions are implemented in this work, where samples are treated separately via physical or chemical methods, described in detail in the following paragraphs, or alternatively with both of them.

3.2.1 Physical Techniques

The physical technique employed to remove the nanosatellites is a thermal treatment based on the low adhesion of the nano-agglomerates to the underlying silica substrate. The samples are immersed in a solution of Saline Sodium Citrate (SSC) and Milli-Q water with 4X salt concentration. Alternatively, the very same procedure can be performed with Phosphate Buffered Saline (PBS) in 4X concentration (where the "X" factor simply indicates that the solution is in a concentrated form that must usually be diluted to a "1X" concentration for use) instead of SSC. The sample in saline solution is left inside an oven at a temperature of about 70 °C for 24 hours.

The removal of the nanosatellites with this treatment is demonstrated both by SEM images and by optical spectroscopy measurements, showing a narrower and blueshifted peak of the treated sample with respect to the non treated ones (see Figure 3.8).

Moreover, since SSC as a saline buffer is the same that will be employed during some functionalization steps, the physical process has the advantage to condition the stability of the sample.

3.2.2 Chemical Techniques

The second method applyed to remove the nanosatellites byproduct is a chemical wet etching one, based on the action of a *gold etchant* solution containing potassium iodide (KI) and mixed with Milli-Q water in ratio 1:1000 where the sample is immersed for a fixed and controlled time.

Since the treatment is an etching process, the samples are successfully cleaned from the nanosatellites, but on the other side, the etching affects the nanoprisms as well, above all the edges and tips of the nanostructure, which are more rounded and less sharp then the untreated or physically-treated samples.

Moreover the gold etchant action is strong and not easy to control and stop, thus requiring precision in the time exposition to prevent an excessive etching, and extremely abundant rinsing in water to stop the action. If these conditions are not rigorously controlled, it is easy to compromise the quality of the nanostructure or to loose stability, with samples showing a continuous etching effect in time, as recorded by a blueshift of the absorbance peak over the time, an undesirable effect not present after the physical treatment.

However, comparing at the absorbance spectra of the sample subjected to physical and chemical treatment in Figure 3.8, it is clear that the second one is much more powerful, and ensure performances quality unattainable with a purely physical treatment. Moreover, precision in the control of the crucial treatment parameter, as described below, lead to satisfying results, without spoiling the sample or loose its time stability.

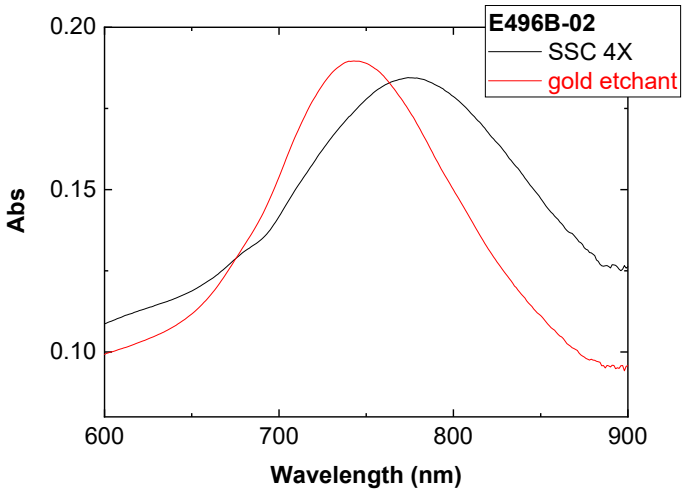

Figure 3.8: Comparison of physical and chemical post-treatment. The absorbance spectrum after the chemical treatment in gold etchant solution for 1 minute leads to a much more sharp and less broadened peak, making the chemical treatment the most suitable to ensure optimal sensing performances.

Chapter 4

MicroRNA Biosensing

Among many different biomolecules of interest in medical and diagnostic sensing, *microRNAs* (miRNAs) have recently gained a major role for their presence and associated functions in patients affected by several diseases [35], [36], [37]. A microRNA is a small single-stranded non-coding ribonucleic acid (RNA) molecule containing about 22 nucleotides whose presence can be observed in plants, animals and viruses.

The primary function of miRNAs is associated to the regulation of RNA stability and translation, since they act on RNA silencing and regulation of gene expression. For this reason, these small filaments have important biological functions, related for example to cell proliferation, survival, migration, invasion, and metastasis in various cancers.

In other words, miRNAs are to all effects biomarkers for many disease (in particular but not exclusively tumoral ones), and small concentrations of the molecules can be detected in biological fluids such as blood, plasma or cerebrospinal fluid. Hence the crucial importance of the development of selectively, sensitive and label-free biosensors able to quantitatively detect small molecules concentration in the complex environment where they are found [38].

As pointed out, the present work is precisely devoted to the fabrication and test of label-free, selective LSPR plasmonic biosensors, able to detect low concentration miRNAs molecules with high sensibility and to obtain quantitatively information on bio-molecular interaction reaction.

Once the design and nanofabrication of the samples was described, all the experimental results and analysis will be presented in the present and following chapters. Nevertheless, before moving to the results of the biosensing experiments, it is essential to give detailed information on the experimental optical measurement setup and its working principle, as well as for the data acquisition and elaboration and the employed functionalization protocol of the samples.

4.1 Optical Measurement Setup

The experimental setup used to perform sensing experiments is placed on an optical bench, mechanically isolated from environment to avoid any form of perturbation caused by vibrations and movements. A picture of the setup with all its components is shown in Figure 4.1.

The light source is a halogen bulb (OSRAM HLX, $12V$ voltage, $75W$ power) electrically connected to a DC voltage generator. A potentiometer is inserted to modify and tune the current flowing in the circuit, thus decreasing or increasing the intensity

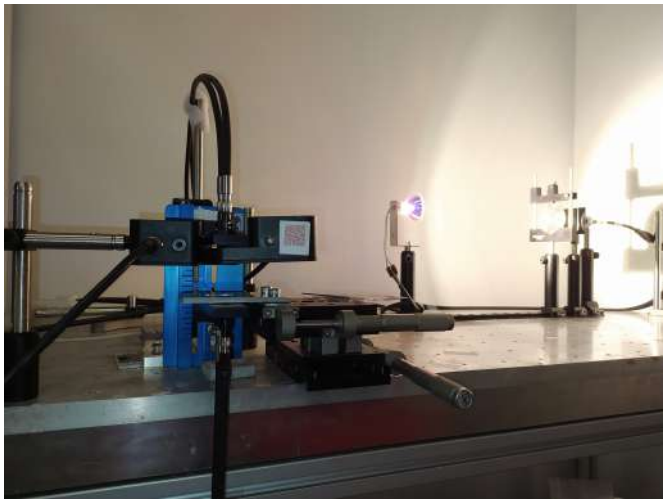

Figure 4.1: Optical bench for the experimental measurements.

of the lamp. The light emitted by the source travels through a converging lens that collimates and direct it to an optical fiber. In addition, a longpass colored filter is placed between the lens and the optical fiber so that light is selectively transmitted in a particular spectral range, with passing light above a wavelength threshold only, called cut-off wavelength.

Ligth travels into the fiber to reach the sample, impinging onto it at normal incidence with unpolarized light configuration.

The sample holder is a platform movable along the two planar directions, provided with three precision micrometers allowing accurate positioning inside the reference system. The need for micrometric precision in the sample illumination and positioning derives from the intrinsic nanometric non-homogeneity of the substrate pattern (i.e., of the colloidal mask), thus requiring that the very same region of interest is investigated during all the steps of consecutive functionalization and measurements of a sample, allowing a meaningful comparison of the data.

For the same issue the actual biosensing surface of a sample is limited (during metal deposition) to a spot of $2mm$ diameter, i.e., the same area of the incident light beam.

The light transmitted through the sample is collected by a second optical fiber connected to a spectrophotometer (Ocean Optics HR 4000 spectrometer) that covers the range 200-1100 nm. The device analyzes the intensity of the input light beam on it as a function of wavelength and gives as output the absorbance/transmittance characteristic spectrum.

The absorbance spectrum peak position is the main parameter of interest in the present work, and the data analysis is based on its determination and control.

4.1.1 Data Analysis

The spectrophotometer is set to acquire percent transmission spectra, that are then converted to percent absorbance spectra following the simple relationship:

$$A = 100(2 - log_{10}(T)) \tag{4.1}$$

The estimate of the wavelength peak λ_{LSPR} can be obtained following three methods.

The first idea is to identify the peak position with the barycenter, $\lambda_{LSPR}^{\text{centroid}}$, of the curve in a fixed region. To fix the extremes of the range in terms of wavelength, the maximum of the curve and the relative minimum on its right are found and an absorbance threshold A_{th} is fixed as a percentage of the absorbance difference between maximum and minimum. All the points A_i near the maximum whose absorbance is higher than fixed threshold are selected and a weighted average of the wavelengths λ_i is computed, with weights given by the normalized absorbance, $(\mathrm{A}_i - \mathrm{A}_{th})$:

$$\lambda_{LSPR}^{\text{centroid}} = \frac{\sum_i \lambda_i \cdot (\mathrm{A}_i - \mathrm{A}_{th})}{\sum_i (\mathrm{A}_i - \mathrm{A}_{th})} \tag{4.2}$$

The other two methods are more rigorous and physically meaningful, since they rely upon a data fitting. Once the threshold and range are fixed in the same way as before, the fitting function is selected.

The first option is to assume an ideal and symmetrical Lorentzian shape of the resonance peak, resulting in the relation between absorbance y and energy x (properly converted from wavelength) given by:

$$y(x) = y_0 + \frac{2A}{\pi} \cdot \frac{w}{4(x - x_c)^2 + w^2} \tag{4.3}$$

where x_c is the Lorentzian peak position.

The second option is to interpret the peak as a Fano-like resonance:

$$T(\lambda) = T_0 + A\frac{q + \sigma\left(\frac{1}{\lambda} - \frac{q\cdot\sigma - \lambda_{LSPR}}{q - \sigma\cdot\lambda_{LSPR}}\right)^2}{1 + \sigma^2 \cdot \left(\frac{1}{\lambda} - \frac{q\cdot\sigma - \lambda_{LSPR}}{q\cdot\sigma\cdot\lambda_{LSPR}}\right)^2} \tag{4.4}$$

where λ_{LSPR} is the wavelength peak, σ its width and q is the Fano parameter.

The Fano resonance is a type of resonant scattering phenomenon characterized by an asymmetric line profile. The asymmetry originates from a close coexistence of resonant transmission and resonant reflection, and can be reduced to the interaction of a discrete (localized) state with a continuum of propagation modes [39].

All the three estimations give good results and, taking into account that sensing performances are associated to peak shift instead of absolute peak positions, they are all in perfect agreement. However, since the Fano function is the best fitting one and it clearly describes the resonant behaviour, it is chosen as the more reliable method and will be applied through the whole work.

4.1.2 Microfluidic Chambers

Since many of the performed measurements refer to the sample interfaced to a liquid solution, the realization of microfluidic chambers is necessary to deliver the solution to the active region of the biosensor in a controlled, dynamic way.

The microfluidic chamber is fabricated starting from a slide of *soda-lime glass* (SLG) of the same dimension of the sensing substrate. The slide is drilled in two points at a distance of about $0.8mm$ and then cleaned, immersed in acetone and sonicated in ultrasonic bath for ten minutes.

A small quantity of Polymethyl methacrylate (PMMA) diluted with the corresponding curing agent in ratio 10:1 is prepared and used to uniformly cover the substrate, which is placed over a hot plate until the polymer layer (of approximately $1mm$ thickness) completely solidifies.

A scalpel is used to create the chamber, removing the PMMA at the drilled holes, at a circular spot of $3mm$ diameter between the two holes, at the regions on both side of the spot and at the thin interspace connecting the capillars with the main spot shaped chamber. The microfluidic chamber has a volume $V = 0.5\mu L$.

Finally, two microfluidic capillars are attacched to the chamber using a UV adhesives for optics (NOA) solidified with a UV lamp. The final result is shown in Figure 4.2.

Figure 4.2: Microfluidic chamber.

The obtained configuration allows the delivering of a solution, through a microsyringe and the capillars, to one of the four spot of a sample that is used as the actual sensing surface for a measurement, while the adjacent ones are preserved both by unwanted functionalization and damaging and can be thus employed in a separate experiment session.

4.2 Functionalization Protocols

One of the biggest challenges for the development of best-performing label-free biosensors is to adopt a functionalization strategy suitable for each biomolecule that is to be detected as target molecule. Fundamental criteria are the high binding affinity between target molecule and bioreceptors of the sensor, high selectivity to avoid aspecific binding and to ensure good performances even in complex and various environment, and label-free functionalization strategy.

In the present study, the target miRNA molecule is the miR27a, a sequence of 21 nucleotides whose characteristics are reported in Table 4.1 together with the specs of the miR27a probe molecule.

The functionalization protocol for the detection of the miR27a target is adapted from the work of Biscontin et al. [40] thanks to a collaboration with their group at the Biology Department of the University of Padova, and is composed of three steps. The first stage of functionalization with a self-assembled monolayer (SAM) of thiols molecules promote the subsequent binding of the bioreceptor, referred to as probe, which finally binds to the target via hybridization reaction (schematical representation in Figure 4.3).

Biomolecule	Sequence	MW (Da)
miR27a probe	GCG GAA CTT AGC CAC TGT GAA	7389.2
miR27a target	TTC ACA GTG GCT AAG TTC CGC	6398.2

Table 4.1: Sequences and molecular weight (MW) of miR27a probe and target oligonucleotides.

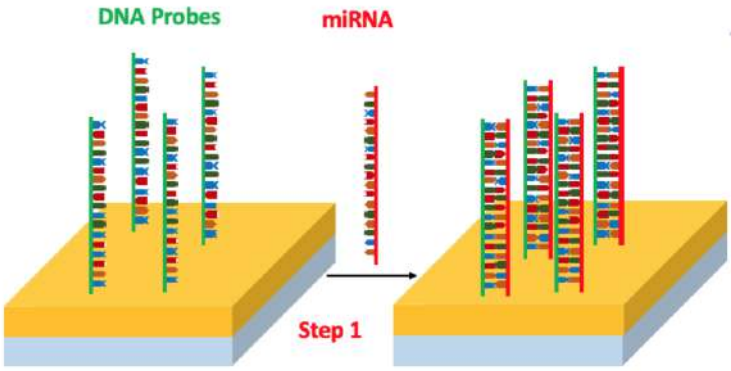

Figure 4.3: Illustration of functionalization steps for miRNA detection. The thiolated nanostructured gold surface of the biosensor is covered with probe moecules acting as bioreceptors to promote the target molecule binding.

4.2.1 Thiols Functionalization

The most widely used strategy to promote the binding of molecules layer onto gold surfaces is the self-assembled monolayer (SAM) of alkanethiols. A thiol is a organosulfur compound of the form $R-SH$, where the $-SH$ functional group is referred to as *thiol group* or *sulfhydryl group* and R is an organic component, which is an alkyl group C_nH_{2n+1} in case of alkanethiols, eventually bound to a further group $-X$.

Thiols functionalization is a consolidated technique since the sulfhydryl group spontaneously bind to Au atoms in a strong and steady binding. On the other side, the second end $-X$ of the thiols molecule can be properly engineed to adapt to the selected bioreceptors.

The SAM of thiols used in this work is actually a mixture of two different alkanethiols (schematic representation in Figure 4.4). The first is the reactive thiol 11-Mercaptoundecanoic Acid (11-MUA) $(HS-(CH_2)_{10}-COOH)$, whose terminal group allows the consecutive probe binding thanks to the crosslinking reaction of the carboxyl group with the end of the probe molecule, while the second one is the inert thiol , 1-Octanethiol (1-OCT) $(HS-(CH_2)_7-CH_3)$. The two types of thiols are respectively added in a ratio of 3:1.

Figure 4.4: 11-MUA and 1-OCT thiols representation.

The differentiation is due to the steric hindrance of the target molecule, which requires a spacer molecule as the 1-OCT, able at the same time to avoid aspecific binding on the surface of the sensor.

The functionalization itself takes place immersing the substrates in an ethanol-based solution with 11-MUA and 1-OCT molar concentration respectively of $0.01M$

and $0.03M$. After the incubation, samples are rinsed first with ethanol and then with Milli-Q water and finally dried with N_2 flow.

4.2.2 Probe Functionalization

The probe molecule is the real bioreceptor of the sensor, i.e., the molecule that will bind to the target miR27a and has to be attached through the thiols layer to the gold surface. The proble used in this work is a single-stranded DNA (ssDNA) of 21 nucleotides and molecular weight of $7389.2Da$ (Table 4.1) whose next hybridization with the target to forme a double-stranded (ds) complex is to be detected.

The probe oligonucleotide is properly modified on one end in order to react with the 11-MUA terminal group and be bound to it. Thus the probe sequence is modified with an amino functional group at the 5' end to promote the thiols binding. Moreover, the used probe molecule is provided with a fluorescent dye, the Cy3, that makes possible to perform fluorescence measurements to investigate the occurrence of binding events. Nevertheless, in this work the dye presence is needless, since no fluorescence measurements are made.

The functionalization protocol to achieve the crosslinking reaction with the 11-MUA covering layer starts with the preparation of the solution containing the probe in which the substrates are incubated.

The buffer for the probe solution is the 2-(N-Morpholino)EthaneSulfonic acid sodium salt (MES) solution with an acid pH of $4.5 \div 5$. The other component is a catalyst, the 1-Ethyl-3-[3-Dimethylaminopropyl]Carbodiimide hydrochloride (EDC), with molecular weigth of $191.7 g/mol$ used in $10 mg/mL$ concentration.

A volume of $200\mu L$ of solution with probe concentration of $4\mu M$ is obtained mixing $152\mu L$ of MES, $40\mu L$ of EDC and $8\mu L$ of probe and is spilled on a hybridization gasket slide, over which the sample is placed face down and properly enclosed, as can be seen from picture in Figure 4.5.

(a) (b)

Figure 4.5: Hybridization gasket slide used for probe functionalization.

After an incubation of one hour, the sample is rinsed consecutively with $0.1M$ MES, $0.02X$ TWEEN, $0.1X$ SDS and Milli-Q water and dried with compressed air flow. This gentle rinsing is performed to prevent the dissociation of the probe from the thiols.

4.2.3 Target Hybridization

The target hybridization spontaneously takes place exposing the probe functionalized substrates to the miR27a target, since complementary nucleotides of the two

sequences bind together via hydrogen bonds.

As for the probe, a target solution is prepared, using as a buffer the SSC $3X$ solution in a proper ratio with the target to obtain the desired concentration. The functionalization can be in principle made with the same procedure employed for the probe, using a hybridization chamber where the incubation takes place for a precise duration. However, as will be explained in the next chapter, the functionalization takes place for a single spot at a time within the fabricated microfluidic chamber. This will allow both to treat and functionalize the spots of a sample independently and to acquire measurements in a real-time mode to follow the dynamics of the hybridization.

Once the hybridization reaction is fully occurred, the rinsing of the sample in water is of crucial importance and has to be made with extreme care and rapidity, immersing the sample in Milli-Q water for one second and drying with N_2 flow. Prolonging the operation would lead to the dissociation of the double strand and loss of all the information. On the other hand a shorter cleaning step would leave the sample covered of impurities and residues of the saline buffer solution (more detailed discussion at the end of the chapter).

4.3 Characterization and Sensing Performances

In the present section the results obtained from sensing experiments are discussed. First the samples are characterized via AFM microscopy, obtaining accurate informations on their characteristic dimensions, then the experimental results are presented and analyzed to extract quantitative performance parameters.

4.3.1 Microscopy Characterization

Once the substrates are nanofabricated, they are first characterized via microscopy measurements. AFM images were acquired to ensure both the homogeneity and uniformity of the NPAs pattern and the correctness of the height of the nanotriangles, of the order of $70nm$. Typical AFM images are reported in the previous Chapter 3.

As it can be seen, the nanostructured samples are sharp and well defined, with few line defects or dislocations that are unavoidable for the NSL nanofabrication technique.

The effect of functionalization on their surface was also investigated, since the thickness of the deposited layer after each functionalization step is an important parameter both to obtain local sensitivity estimates and to study the molecules dimension as adsorbate layer.

Since the involved molecular dimensions are of the order of $1 - 10nm$, the nanostructured surface is not the best substrate to allow the detection of these thick layers with the resolution of an AFM microscope.

For this reason, an empirical model for the bound molecules was built starting from a planar uniform Au surface without nanostructured morphology. To this aim, silicon substrates were properly cleaned and covered with Cr and Au uniform thin film layers via thermal evaporation metal deposition. Since Cr layer simply serves as adhesion layer and Au does not require a specific thickness, they were deposited respectively for $5nm$ and 100 in nominal height.

Functionalization protocols described above were used for silicon substrates and AFM images were acquired between a step and the following one and analyzed.

The data obtained for each layer thickness are reported in Table 4.2 for two functionalized silicon samples:

Sample	Thiols (nm)	Probe (nm)	Target (nm)	t_{probe} (nm)	t_{target} (nm)
E498C	117.4 ± 0.6	123.3 ± 0.5	125.0 ± 0.6	5.9 ± 0.8	1.7 ± 0.8
E499B	106.4 ± 0.3	111.0 ±0.5	112.4 ± 0.5	4.6 ± 0.6	1.4 ± 0.7

Table 4.2: Experimental thickness values extracted from AFM measurements. The first three columns refer to the overall height of the samples after the correspondent functionalization step; the last two columns report the resulting thickness value associated to probe and target functionalization layer respectively.

The obtained mean value of probe and target thickness are respectively

$$t_{probe} = 5.3nm \pm 1.0 \qquad t_{target} = 1.6 \pm 1.1nm \tag{4.5}$$

and they are compatible with literature results [41] as expected.

4.3.2 Biosensing Experiments

Biosensing tests were carried out monitoring the absorbance spectrum of a sensing spot and its peak position. Measurements are performed over the sample in air, free from microfluidic apparatus, at the beginning, just after the nanofabrication and after the chemical post-treatment (all the samples were treated with gold etchant solution for 1 minute, as explained in section 3.2), and then three times after each functionalization steps (thiols, probe and target).

Since the self-assembled monolayer of alkanethiols has an approximate thickness of few nanometers (about $2nm$), as expected the peak spectral shift is not detected with the available samples and experimental setup, as can be seen from the two spectra exactly superimposed. Moreover, this does not represent a problem, since the meaningful differential measurements associated to the sensing output are the shift produced from probe and, above all, target binding.

Thus, for each sample in the following, the reported spectral shift are always referred to the difference between the final peak position and the initial peak of the thiolated sample, used as reference starting point.

The experimental results of miR27 target detection are shown for the sample E488B-02, which was functionalized with target concentration of $2\mu M$.

The observed peak shifts are for probe binding and for the analyte detection are respectively:

$$\Delta\lambda_{LSPR}^{probe} = 5.6 \pm 0.04nm \qquad \Delta\lambda_{LSPR}^{target} = 4.0 \pm 0.04nm \tag{4.6}$$

For the estimate of the bulk sensitivity, the sample is covered with the fabricated microfluidic device, whose chamber is left initially empty and then filled with Milli-Q water. The observed spectral shift $\Delta\lambda_{LSPR}$ and the difference of refractive index $\Delta n_s = n_{H_2O} - n_{air}$ of air ($n_{air} = 1.00$) and water ($n_{H_2O} = 1.33$) lead to a direct valuation of the bulk sensitivity, evaluating the expression 2.3 discretizing both the numerator and denominator with the absolute differences. The parameter results in:

$$S_\infty = \frac{\Delta Y}{\Delta n_s} = 217nm/RIU \tag{4.7}$$

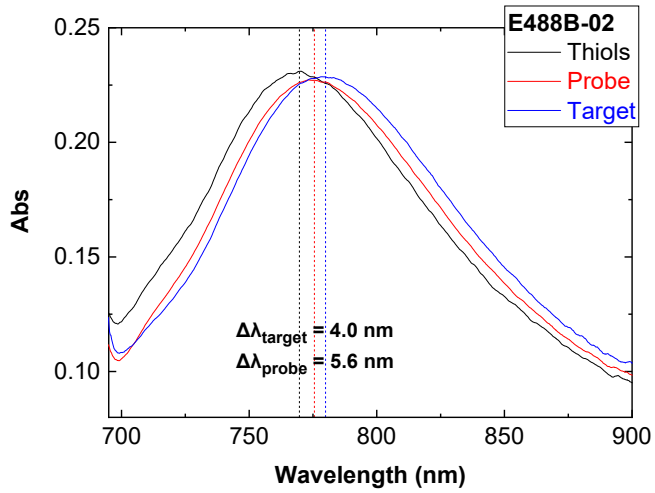

Figure 4.6: Absorbance spectra after each functionalization step. The vertical dashed lines show the redshift of the peak at each step, whose values are shown.

4.3.3 Biosensor Regeneration

One of the possible challenging sensing issues is the regeneration of the sensor. An ideal biosensor, among the other performance properties, can be a regenerable and reusable device, allowing multiple uses without compromising sensing efficiency.

To accomplish this task, a proper cleaning and regeneration process is needed, carried out according to a protocol able to entirely remove the target molecules on the surface of the sensors and, at the same time, preserving the bioreceptor (probe) binding. In fact the unwanted unbinding of the bioreceptors of the sensor, would imply the alteration of the sensing properties, without the receptors to which the target should be bound, and for this reason the need of a new functionalization step that would affect the sensing behaviour, compromising it.

Some tests were performed to check if the rinsing stage at the end of target functionalization can compromise itself the sensing properties of the biosensor or can be modified to obtain a reusable sample with the same characteristics as before the target hybridization on its surface.

What emerged is that the employed rinsing procedure is the minimum necessary to clean the sample from saline soltion residuals, that otherwhise remain on the sample surfaces forming a halo over the spot.

Regarding the regeneration, it was found that immmersing the sample in water for at least 10 minutes leads to the complete unbinding and removal of the target molecules, while the probe binding is strong enough to not to be affected at all by the cleaning process.

This can be clearly seen from Figure 4.7, where the absorbance peak of a spot is recorded immediately after the probe functionalization, when the surface is not yet exposed to the target solution, and again after the target functionalization in $0.1\mu M$ concentration and the subsequent 10 minutes washing in Milli-Q water.

As pointed out, the two spectra are exactly superimposed and no shift is observed in both directions.

Stress tests were finally performed conducting the rinsing in warm water, at a temperature of 50 °C for the same duration. As before, the regeneration of the sample is

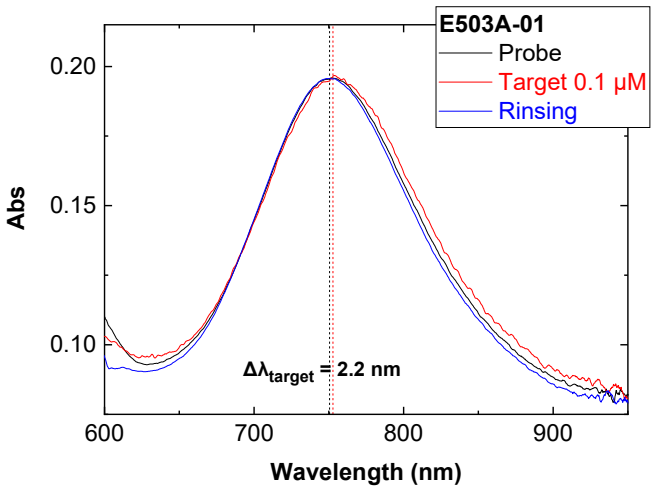

Figure 4.7: Regeneration test on sample E503A, spot 01. The absorbance spectra are showed in order after probe functionalization with no target, after target functionalization with concentration of $0.1\mu M$ and after the 10 minutes rinsing in water.

achieved avoiding probe dissociation.

These results are a good evidence of the proper regeneration and reuse possibility of the plasmonic biosensors realized in the present work. Interesting future issues to be investigated are the maximum number of use of a single spot of the biosensors, meaning how many times the same sensor can be used to conduct sensing experiments without loosing efficiency, and a functionalization procedure for the probe binding that ensure strength and stability even with a cleaning procedure deeper than the one adopted.

Chapter 5

Dynamic Biosensing

Hybridization of complementary DNA and RNA sequences or single strands of DNA is a fundamental molecular recognition process widely exploited for diagnostic, biotechnology and nanotechnology applications.

The thermodynamics of hybridization has been well studied, and algorithms based on the nearest-neighbour model of base stacking predict minimum free-energy structures and melting temperatures with reasonably good accuracy. In contrast, the kinetics of hybridization remain poorly understood, and no models or algorithms have been reported that accurately predict hybridization rate constants from sequence and reaction conditions. Moreover, the lack of information affecting DNA interactions in bulk solutions highly increases in the modelling of the same interactions on a surface, upon which are based the most common approaches of immobilization of single stranded DNA probes that bind complementary targets in solution.

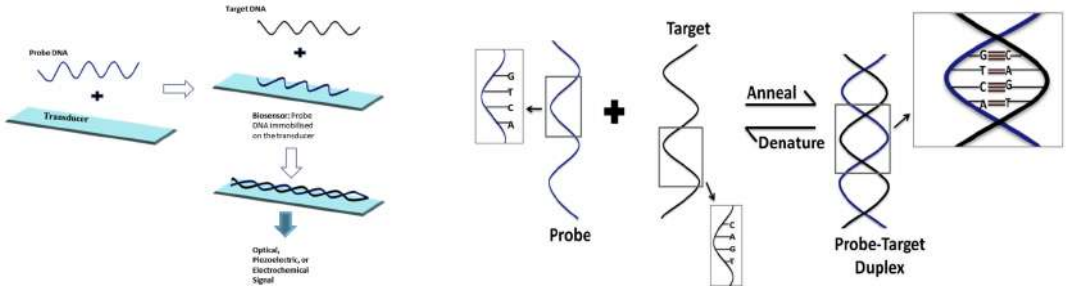

(a) (b)

Figure 5.1: Schematic illustration of the underlying concept in DNA hybridization biosensors (a) and of hybridisation of complementary nucleotide bases in a probe-target duplex (b).

This deficiency has impacted the research field, requiring new methods and technologies to tackle the problem.

In the present work NPAs LSPR-based biosensors, previously employed for static detection of miRNA target molecules, are exploited in a microfluidic configuration in order to dinamically investigate the hybridization kinetics of the same target sequence [42], [43].

In the following section, the modifications of the measurement setup and data management and elaboration will be described; then the experimental results are shown together with their analysis and implications.

5.1 Setup and Data Elaboration

The optical setup for dynamic measurements is the same used for static detection tests (described in section 4.1) to which some changes are made.

Since the purpose of the dynamic measurements is to control in real time the spectral absorbance wavelength peak for different time intervals, the stability and synchronization of the measurement apparatus is an essential condition. Nevertheless, the halogen bulb is intrinsically a non homogeneous and steady light source, whose employment assure optimal performances in terms of speed and light intensity counts, not ensured by others light source, but is not suitable as a stable baseline signal.

For these reasons a double channel acquisition system was designed. A two-core fiber optical cable is substituted to the classical one-core fiber of the previous section, splitting the input light signal in two different paths.

Two programmable shutters are placed between the sample holder and the output end of the optical fiber, one for each separate channel. A second couple of independent optical fiber is connected from the other side of the sample holder to the Ocean Optics spectrophotometer, to collect the transmitted light and to analyze the spectral response as done before.

A detailed view of the optical apparatus in proximity of the sample is shown in Figure 5.2, where the shutters, the input and output couple of optical fiber and the two corresponding light channel (sample channel and reference, or baseline, channel in the following) are distinguishable.

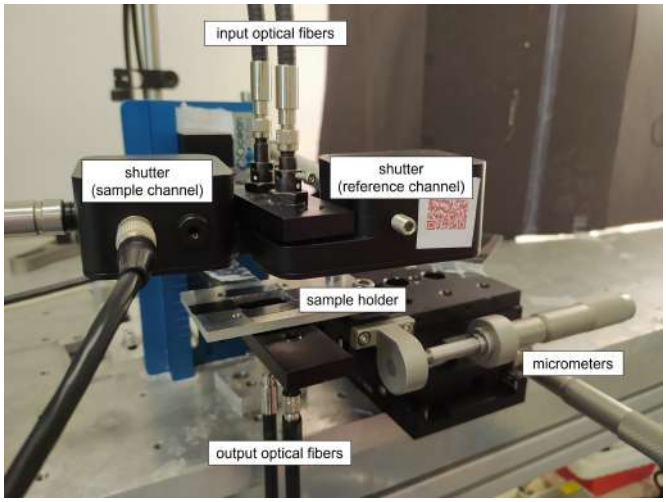

Figure 5.2: Zoomed view of the optical measurement setup with detailed view of the shutters and the two light channels.

A different, simplified optical fiber system was tested before proceeding with the experiments, using a single-core cable that splits in two at the end. This configuration provides a desirable balance in the intensity signals of the two different channel, but is affected by high intensity losses that strongly decrease the output intensity.

The two-core fiber optic system, on the other hand, preserves the quality and intensity of the input signal and the unbalance of the two channels can be monitored and easily compensated with a proper tuning of the optical fiber anchoring.

The data acquisition is performed through a loop acquisition with two adjustable parameters: the *average parameter* defines the number of average operations to be carried out for the acquisition spectrum, while the *time acquisition interval* fixes the

time lapse for a spectrum acquisition, coincident with the aperture time of the shutter over the respective channel.

The controlled loop process thus acquires the transmission spectrum alternatively for the sample channel, reference channel and dark (corresponding to shutter closure) and saves the data in properly labeled files. The very first spectrum for the sample channel is measured for a baseline region of the sample, that means over a blank area of the microfluidic chamber exactly near the spot; after that the micrometers system allows the repositioning over the spot and all its consecutive spectra acquisition.

Then a Python script is used to elaborate and analyze the data, with the possibility to perform these operations both real time during the acquisition or separately in a post processing.

The first data elaboration operation consists in the correction of the transmission spectra to take into account the time instability of the light source. The transmittance T_t at time t is in principle given by the ratio between the sample signal at time t S_t and the signal of the sample baseline (blank sample surface) B_t, both corrected subtracting the dark signal at the same time D_t (that is assumed identical for the two channels).

$$T_t = \frac{S_t - D_t}{B_t - D_t}. \tag{5.1}$$

However the baseline signal at time t is a missing data, since it is acquired only at the beginning of the loop and a live measurement would require a continuous manual movement of the sample holder to center alternatively the spot sensing area and the near baseline blank region. The used setup allows instead to correct the acquired data thanks to the live monitoring of the light source through the reference channel. In fact, if R_t stands for the signal of the reference channel at time t, the following relationship holds:

$$\frac{B_t - D_t}{B_0 - D_0} = \frac{R_t - D_t}{R_0 - D_0} \tag{5.2}$$

and the final corrected value of the transmittance over the time immediately follows and can be easily computed as:

$$T_t = (S_t - D_t) \cdot \frac{(R_0 - D_0)}{(B_0 - D_0)(R_t - D_t)}. \tag{5.3}$$

Once the transmission spectra are properly corrected, the temporal peak position is monitored associating to each spectrum its temporal reference and wavelength peak and plotting into a graph the observed trend.

5.2 Results and Analysis

Binding kinetics measurements are performed recording the absorbance wavelength shift of a sample as a function of time. The initial absolute peak position is chosen as reference zero value, expressing the kinetics curve as the temporal peak shift instead of absolute peak position.

The acquisitions were carried out testing different target concentration and, for each measurement, an early time lapse is recorded with the microfluidic chamber covering the spot filled with saline buffer solution SSC $3X$. Once the sample immersed in solution is stabilized, no spectral shift is observed, as expected, since the system at the nanoscale is in equilibrium and no reactions happen at the surface of the plasmonic nanoarray.

After this initial stability time interval, the target solution with a fixed concentration is injected into the microfluidic chamber until it is filled. The hybridization reaction between the probe and miR27a target at the surface of the biosensor produces as output a rapid redshift in the spectral peak, visible in the kinetics curve as a defined rising in correspondence of the time of injection of the target solution.

The kinetic curve obtained for a target concentration of $2.0\mu M$ is shown below:

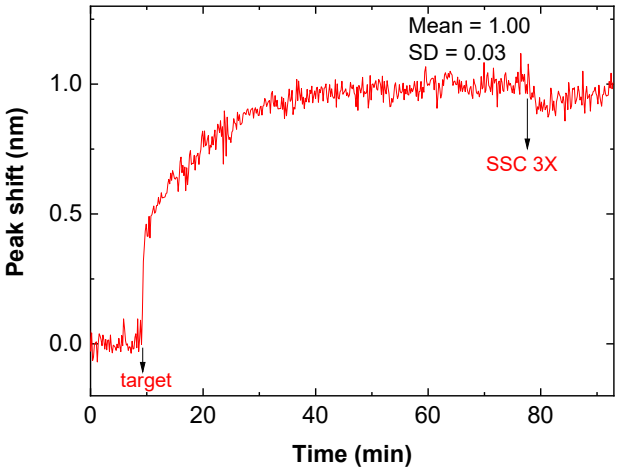

Figure 5.3: Real time output response of the sensor (E488B-02 sample) with target exposition of $2.0\mu M$ concentration. Target and buffer injection time are shown, together with the observed mean peak shift.

As evidenced in Figure 5.3, before the dynamic acquisition is interrupted, a further injection of saline buffer is carried out as a protocol step. The buffer exposure is a required stage to prove both that the redshift signal produced by the target binding is a consistent response of the biosensor, due to the successful target detection instead of other possible causes, and that the target is irreversibly bound to the bioreceptors covering the plasmonic surface, with a binding strength high enough to ensure sample stability. Otherwise a negative peak shift should be observed, with restoration of the initial peak position or any other response revealing no physical meaning of the observed shift after the target injection.

The overall spectral shift after the target exposure can be computed as the difference between the initial and final peak position, where the two values are computed averaging the experimental points in the initial and final stability range. The result in the case of the $2.0\mu M$ target concentration above is a spectral shift of:

$$\Delta\lambda_{target} = 1.00 \pm 0.03nm. \tag{5.4}$$

The same result can be obtained comparing the initial and final absorption spectra of the acquisition in Figure 5.4 and statically observing the wavelength redshift.

The first tested concentration was chosen of $2.0\mu M$ since, considering the characteristic surface dimensions both of the nanostructured sensor and of the self-assembled monolayer of thiols bound to gold atoms, this value ensure the saturation of all the available binding sites.

It is possible to estimate the gold area exposed by a single NPA spot, starting from the total surface of a single nanoprism, that results $A_{prism} \simeq 0.019\mu m^2$. Since a spot

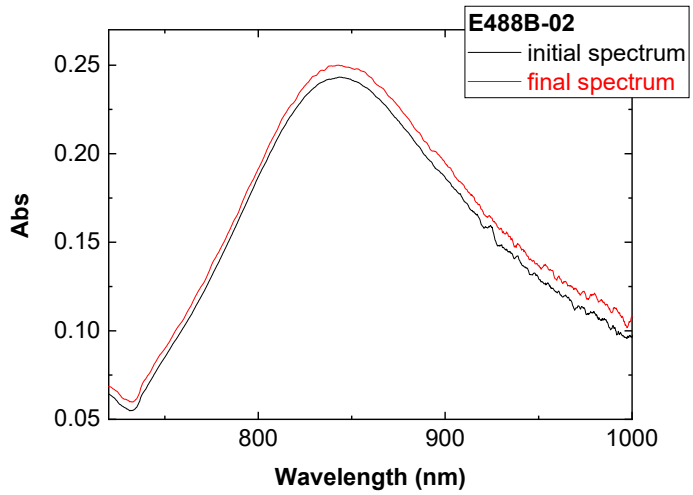

Figure 5.4: Initial and final absorption spectra of the dynamic acquisition in Figure 5.3.

includes about $2.66 \cdot 10^7$ nanoprisms, the total gold area per spot is $0.505mm^2$. Since the footprint of a single thiol molecule is $A_{thiol} \simeq 0.214nm^2$, the number of total thiols over one spot is $N_{thiols} \simeq 2.36 \cdot 10^{12}$, $0.59 \cdot 10^{12}$ 11-MUA thiol and $1.77 \cdot 10^{12}$ 1-OCT thiol. As a consequence, the number of probe molecules needed for the saturation of the sensing surface is $0.59 \cdot 10^{12}$. This molecules number is by far ensured by the functionalization with probe in $4\mu M$ concentration. Indeed, taking into account the volume $V = 0.5\mu L$ of the microfluidic chamber and the target concentration of $2.0\mu M$, it follows that the available number of target molecules is $0.6 \cdot 10^{12}$, which exactly corresponds to saturation condition.

5.2.1 Limit of Detection

To further investigate the biosensors performances, a crucial quantitative parameter is the limit of detection (LOD), that represents the lowest values of target concentration detectable with the employed plasmonic biosensors.

To reach this purpose, the same measurement approach in a dynamical regime was employed, repeating the sensing tests gradually decreasing the target concentration. Measurements were acquired for concentration of $1.0\mu M$ and $0.1\mu M$. The obtained results are shown in Figure 5.5 below, and the sensor response in terms of wavelength peak shift are summarized in Table 5.1.

Sample	Target concentration (μM)	Target shift (nm)
E488B	2.0	1.0 ± 0.03
E497B	1.0	0.73 ± 0.05
E503B	0.1	0.20 ± 0.04

Table 5.1: Summary of the sensor shift response at the variation of the target concentration.

By monitoring the response $\Delta\lambda_{LSPR}$ with exposure to different concentration of miR27a target molecule, a sensing curve can be obtained. The experimental data in Table 5.1 were reported in graph, and a fit was performed. The fitting function adopted was the Langmuir isotherm function, since a Langmuir adsorption model is assumed:

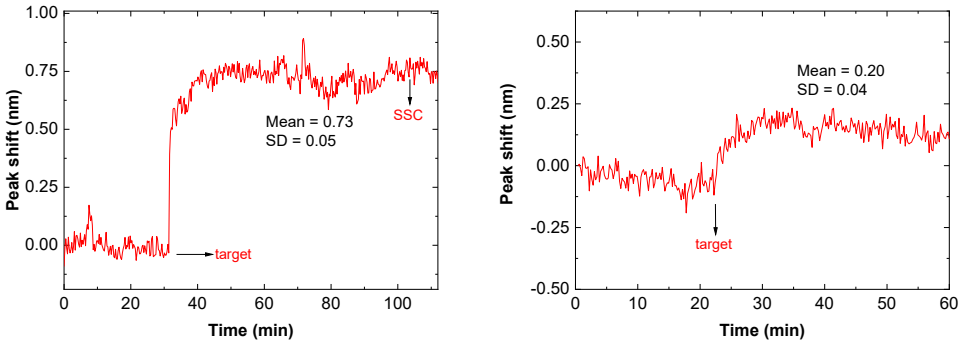

(a) (b)

Figure 5.5: Real time output response of the sensor with two different target concentration, $1.0\mu M$ in figure (a) and $0.1\mu M$ in figure (b).

The Langmuir adsorption isotherm is used to describe the equilibrium between adsorbate and adsorbent system, with the adsorbate adsorption limited to one molecular layer. The isotherm model was first proposed by Langmuir in 1918 [44] and is widely adopted, since it is suitable for describing the chemisorption process when ionic or covalent chemical bonds are formed between the adsorbent and the adsorbate and thus can be extended to several systems.

The Langmuir adsorption isotherm describes the measured signal, $\Delta\lambda$ in the present case, when the steady-state binding is reached, after the injection of analyte concentration C. The model considers the surface as homogeneous, assuming that there is no lateral interaction between adjacent adsorbed molecules when a single molecule occupies a single surface site. The form of the Langmuir equation is:

$$\Delta\lambda = \frac{\Delta\lambda_{\text{sat}} \cdot K_a \cdot C}{1 + K_a \cdot C} \tag{5.5}$$

where $\Delta\lambda_{\text{sat}}$ is the maximum output signal, i.e., the maximum shift when saturation is reached and K_a is the affinity constant between ligand and adsorbate (target).

The fit parameters obtained with no constraints on the maximum shift yielded:

$$\Delta\lambda_{\text{sat}} = (1.3 \pm 0.1)\text{nm} \quad K_a = (1.4 \pm 0.4) \cdot 10^6 \text{M}^{-1} \tag{5.6}$$

with a value for the maximum output signal greater than the one of $1.0nm$ obtained assuming saturation regime. However, a second fit where the condition $\Delta\lambda_{\text{sat}} = 1.0$ was imposed, showed an overall worse goodness of fit and an affinity constant $K_a = (3.8 \pm 1.4) \cdot 10^6 \text{M}^{-1}$ significantly different from the one obtained before. The two results are shown in the following Figure 5.6.

The zero-shift response point shown in graph is to be pointed out, representing not a theoretical predicted data, but a measure itself, corresponding to the absence of shift observed with injection of blank buffer solution with zero target concentration.

Observing the results obtained with both fit conditions, it is to be pointed out as in both case the experimental do not perfectly overlap with the fitting curve, however the trend is clearly well described by the model and it is in agreement with the value of affinity constant that can be found in literature for the DNA hybridization reaction.

Furthermore, two important issues are to be taken into account. First a higher number of experimental points should be acquired and considered, to ensure a more

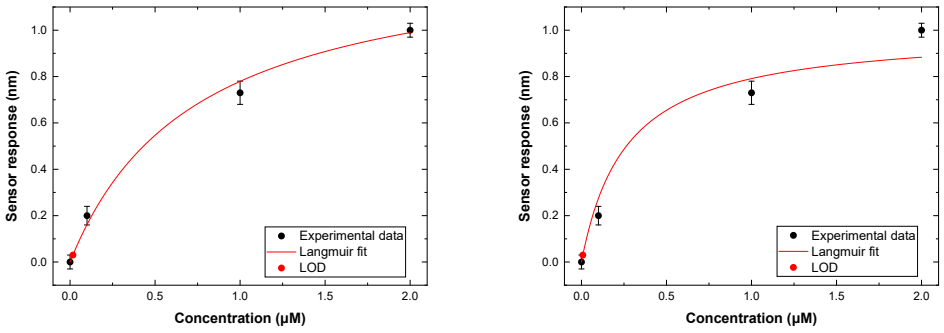

(a) (b)

Figure 5.6: Langmuir sensing curve; the limit of detection is marked as a red point with no error bar.

detailed investigation of the concentration sensing regime, and then for each experimental data of the curve, an interesting option is to take repeated measurements to enrich statistics. The shown data, indeed, derive from single non repeated measurement for each target concentration, and their experimental error is chosen considering the standard deviation of the signal associated to the noise of the kinetic curves instead of the standard deviation of a set of measurements of the same data set. For this reason, the error bars in Figure 5.6 can be slightly underestimate and compromise the overall quality of the fit.

Even so, from the sensing curve the LOD can be detected, considering the intersection between the Langmuir isotherm curve and the error bar given to the shift measurements, equal to $0.03nm$. Considering the Langmuir fit with not fixed maximum response, the limit of detection results $LOD = 0.01\mu M$, which can be expressed in terms of number of moles or as mass/volume ratio, remembering the microfluidic chamber volume and the target molecular weigth ($6398.2Da$):

$$LOD = 50fMoles = 63.98ng/mL. \tag{5.7}$$

The fit obtained with the free parameter $\Delta\lambda_{sat}$ is chosen as the most reliable one, since the agreement of experimental data with the fit curve is much better. Moreover, the constraint over the maximum output response, forced to be equal to the measured value, is a strong assumption, not justified by the single measurement and its uncertainty.

A possible explanation of the difference between the shift output associated to the saturation regime and the value obtained from the fit can be identified for example on the unspecific binding on the sensing surface. Since no strategy was applied during the functionalization protocol as a protection against aspecific binding, it is possible that a signal loss intrinsically affects the sensing performances, leading to underestimated output signal intensities.

5.3 Kinetics of the Hybridization

LSPR biosensors power relies not only on the sensitive and selective detection of analyte molecules, but also on their effectiveness in the determination of the affinity

and kinetic rate constants of biomolecular interactions between an immobilized and a soluble binding partner. Hybridization of complementary single strands of DNA, in particular, represents a very effective natural molecular recognition process widely exploited for diagnostic, biotechnology and nanotechnology applications. However, despite the deep knowledge on DNA interactions in bulk solution, the modelling of the same interactions on a surface are still challenging and perceived as strongly system-dependent [45].

Since the most common approach behind the working principle of plasmonic biosensors is the immobilization on a surface of single stranded DNA probes that bind complementary targets in solution, as in the present work, they are extremely powerful methods to investigate the problem.

The most common binding kinetics model is the ideal pseudo-first-order binding kinetics, also called Langmuir-like behaviour [46].

The association and dissociation kinetics are in this framework described by single-exponential time courses of the sensor output signal $F(t)$:

$$F(t) = a \cdot \left(1 - \exp\left\{-k_{ON}^{obs} \cdot t\right\}\right) \tag{5.8a}$$

$$F(t) = a \cdot \exp\left\{-k_{OFF} \cdot t\right\} \tag{5.8b}$$

where a is the output signal once equilibrium is reached and k_{ON}^{obs} is the observable rate constant of the association curves. This parameter scales with the analyte concentration C according to the expression

$$k_{ON}^{obs} = C \cdot k_{ON} + k_{OFF} \tag{5.9}$$

with k_{ON} being the intrinsic molecular on-rate and the dissociation rate k_{OFF} is independent on the concentration. These two constants define the kinetic parameters of dissociation constant $K_D = k_{OFF}/k_{ON}$ and its inverse $K_A = k_{ON}/k_{OFF}$, the association constant, which complete the full kinetic description of the system.

Considering the kinetic curves obtained in the previous section, it is possible to perform a single exponential fit restricted to the time interval of the target exposition, that means from the target injection and immediate sensor response, until the steady-state equilibrium.

The curves are shown together in the same graph, where the dashed lines are the exponential fitting functions.

The agreement between the experimental curves and the expected trend is excellent and the fit exponential function exactly follows the measured trend. Moreover, the time constants $\tau = 1/k_{ON}^{obs}$, corresponding to the inverse of the observable rate constant of the association curves, derives from the fit and are reported in Table 5.2.

Concentration (μM)	τ (min)
2.0	10.2 ± 0.3
1.0	2.7 ± 0.5
0.1	1.7 ± 0.4

Table 5.2: Values of the time constant τ for each concentration kinetic curve, obtained as a fit parameter of the single exponential function.

As it can be noted, the time constant linked to the association equilibrium reaching, increases with the concentration. This trend deviates from what predicted from equa-

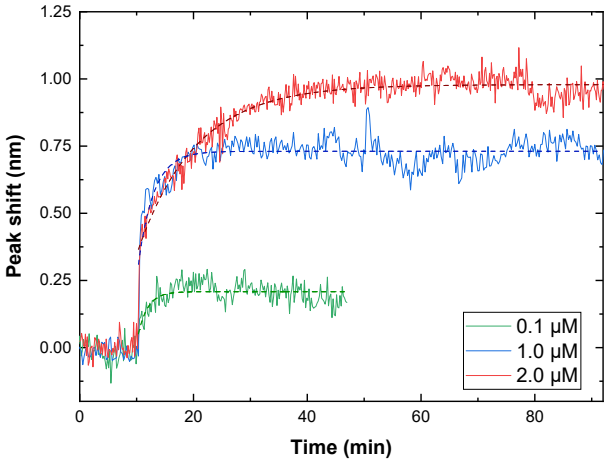

Figure 5.7: .

tion 5.9, if one considers the constancy of association and dissociation intrinsic rate k_{ON} and k_{OFF}, and the linear dependence of k_{ON}^{obs} on C.

This suggests that the ideal pseudo-first-order binding model is not suitable for the description of the system in question. The result is not meaningless or anomalous, since well known evidences are present about the deviation in SPR surface binding kinetics from the ideal pseudo-first-order binding kinetics of bi-molecular reactions.

The two most common sources of this phenomenon are mass transport limitation and the heterogeneity of the surface sites (Figure 5.8), and are intrinsic to the use of a biosensor surface for characterizing interactions [47], [48].

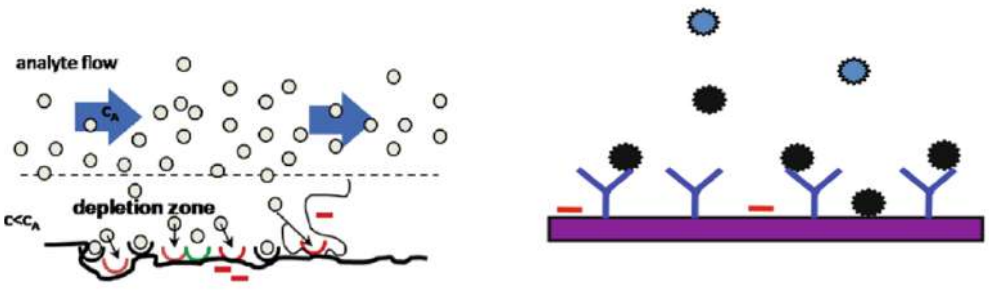

(a) (b)

Figure 5.8: Effect of limited mass transport and heterogeneity sources. In the association phase, limited mass transport causes the analyte close to the surface to be bound more quickly than it can be resupplied by the bulk analyte flow. This creates a depletion zone of analyte at the surface, resulting in a concentration close to the surface lower than the concentration in the bulk (a). Surface site heterogeneity may occur fundamentally from nonspecific binding to the surface [47].

In particular, mass transport of analyte to surface-immobilized affinity reagents is the fundamental bottleneck for sensitive detection in solid support microarrays and biosensors, since analyte depletion in the volume adjacent to the sensor causes deviation from ideal association, significantly slowing down reaction kinetics, and causing

inhomogeneous binding across the sensor surface. To ensure homogeneous binding across a spot-shaped biosensing surface, crucial parameters are found in the flow rate and spot diameter.

Surface heterogeneity linked deviations are often observed as a slow signal increase in what should ideally be a steady-state signal at high analyte concentrations, arising from heterogeneity of the surface sites or heterogeneity of the analyte. Another common feature is the lack of saturation of the steady-state response as a function of concentration, which points to the existence of weaker, possibly nonspecific binding sites.

As a consequence of these challenging issues, for binding studies using surface-based optical biosensing, it is crucial to consider these intrinsic potential problems associated to the presence of a surface and immobilization, to properly design and perform sensing experiments. However, although significant efforts have been devoted in the past decade to create a variety of specific immobilization strategies for creating ideal surfaces, many physical details of the binding surface are still unknown, and thus the heterogeneity of the surfaces and dispersion of affinities of sites generated with these strategies need more investigation.

At the same time, more complex analytical models were developed by researchers to explain features inconsistent with Langmuir-kinetics, proposing interesting non-Langmuir kinetic models, accounting for example for an enhanced electrostatic repulsion originating from the surface immobilization of nucleic acids and for steric hindrance close to full hybridization of the surface probes [49].

As future outlook will be thus interesting and challenging to build a new non-ideal descriptive model, able to quantitatively take into account both mass transport limitation and heterogeneity effects.

Chapter 6

Conclusions and Outlooks

The aim of this work was to realize and test a selective and label-free plasmonic biosensors to study the kinetics of biomolecular binding at the biosensor surface. Results have shown that NSL technique, combined with metal deposition via thermal evaporation, is a cost-effective successful nanofabrication method. It is able to assure low cost production and extended dimension of sensing surface, with wide area of the order of centimeter square showing ordered and defect-free structure. Moreover, the geometric parameters of the nanostructure morphology are well tunable, and a rapid and efficient post-production chemical treatment is sufficient to ensure optimal performances with defined and well-shaped absorbance spectra and a bulk sensitivity of $S_\infty \sim 217 nm/RIU$.

The functionalization strategy of the NPAs structures proved to be a solid protocol for the detection of the miR27 target molecule. The LSPR wavelength peak monitored via optical spectroscopic measurements emerged as sensing parameter whose redshift magnitude across the functionalization protocol steps immediately returns a response proportional to the analyte concentration. The binding event was also successfully detected via AFM microscopy, which made possible to determine with nanometric precision the thickness of each functionalization layer.

Nevertheless, as a future perspective, an improvement of the functionalization procedure is desirable, since aspecific target binding on the non-active region of the NPAs substrate would lead to signal losses and compromise, underestimating them, the quantitative performances of the biosensor. The addition of a protection coating, in addition to repeated measurements of the output response after the exposition to different target concentration in a range finely investigated, will definitively boost the device sensitivity.

However, in the working condition of the present work yet, good results were obtained in terms of limit of detection of the sensor, which results of:

$$LOD \sim 50 fMoles \sim 63.98 ng/mL.$$

The NPAs morphology confirmed to be a powerful structure for the dynamic study of the binding interaction dynamics as well. Hybridization kinetics, in particular, was investigated, and plasmonic biosensors demonstrated extremely valid and accurate candidate to be employed. Time and affinity constants and association or dissociation rate can be easily extracted starting from dynamic measurements acquired real time as the reaction proceed, with the help of a microfluidic chamber.

The experimental data demonstrated a deviation in the association kinetics model from the ideal Langmuir description, with a time constant of the association stage increasing as the target concentration increases. The motivations justifying the deviation

are the two most common ones involved in the deviation in SPR surface binding kinetics from the ideal pseudo-first-order binding kinetics of bimolecular reactions. The first is mass transport limitation, causing the analyte close to the surface to be bound more quickly than it can be resupplied by the bulk analyte flow, and the second is the heterogeneity of the sensing surface, affecting the phenomenon, among the other ways, fundamentally as nonspecific binding to the surface. This last issue is a further proof of the pitfall of the functionalization protocol and of the issues under the determination of the LOD of the present work.

Overall, the plasmonic nanobiosensors demonstrated their strengths and effectiveness in the realization of selective and label-free extremely sensitive biosensors, whose range of application encloses variety of purposes as quantitative biomolecule detection or reaction kinetics investigation.

Bibliography

[1] Stefan A. Maier. *Plasmonics: Fundamentals and applications*. Springer US, 2007.

[2] P. B. Johnson and R. W. Christy. Optical constants of the noble metals. *Phys. Rev. B*, 6:4370–4379, 1972.

[3] Hao Feng and Nordlander Peter. Efficient dielectric function for fdtd simulation of the optical properties of silver and gold nanoparticles. *Chemical Physics Letters*, 446:115–118, 2007.

[4] Yi-Tao Long and Chao Jing. *Localized Surface Plasmon Resonance Based Nanobiosensors*. Springer Berlin Heidelberg, 2014.

[5] Matthew A. Cooper. *Label-Free Biosensors: Techniques and Applications*. Cambridge University Press, 2009.

[6] Barbora Špačková, Piotr Wrobel, Markéta Bocková, and Jiří Homola. Optical biosensors based on plasmonic nanostructures: A review. *Proceedings of the IEEE*, 104:2380–2408, 2016.

[7] M. Fleischmann, P.J. Hendra, and A.J. McQuillan. Raman spectra of pyridine adsorbed at a silver electrode. *Chemical Physics Letters*, 26(2):163–166, 1974.

[8] Bo Liedberg, Claes Nylander, and Ingemar Lunström. Surface plasmon resonance for gas detection and biosensing. *Sensors and Actuators*, 4:299–304, 1983.

[9] Marek Piliarik, Lucie Párová, and Jiří Homola. High-throughput spr sensor for food safety. *Biosensors and Bioelectronics*, 24(5):1399–1404, 2009.

[10] Soler M, Mesa-Antunez P, Estevez MC, Ruiz-Sanchez AJ, Otte MA, Sepulveda B, Collado D, Mayorga C, Torres MJ, Perez-Inestrosa E, and Lechuga LM. Highly sensitive dendrimer-based nanoplasmonic biosensor for drug allergy diagnosis. *Biosensors 'I&' bioelectronics*, 66:115–123, 2015.

[11] Bin Liu, Jinyin Zhuang, and Gang Wei. Recent advances in the design of colorimetric sensors for environmental monitoring. *Environmental Science: Nano*, 7:2195–2213, 2020.

[12] Jing Zhao, Xiaoyu Zhang, Chanda Ranjit Yonzon, Amanda J Haes, and Richard P Van Duyne. Localized surface plasmon resonance biosensors. *Nanomedicine*, 1:219–228, 2006.

[13] Adam D. McFarland and Richard P. Van Duyne. Single silver nanoparticles as real-time optical sensors with zeptomole sensitivity. *Nano Letters*, 3:1057–1062, 2003.

[14] Kerry J. Lee, Prakash D. Nallathamby, Lauren M. Browning, Christopher J. Osgood, and Xiao-Hong Nancy Xu. In vivo imaging of transport and biocompatibility of single silver nanoparticles in early development of zebrafish embryos. *ACS nano*, 1:133, 9 2007.

[15] Jiří Homola. *Surface Plasmon Resonance Based Sensors*. Springer Berlin Heidelberg, 2006.

[16] Haes Amanda J. and Van Duyne Richard P. A nanoscale optical biosensor: sensitivity and selectivity of an approach based on the localized surface plasmon resonance spectroscopy of triangular silver nanoparticles. *Journal of the American Chemical Society*, 124:10596–10604, 2002.

[17] Linda S. Jung, Charles T. Campbell, Timothy M. Chinowsky, Mimi N. Mar, and Sinclair S. Yee. Quantitative interpretation of the response of surface plasmon resonance sensors to adsorbed films. *Langmuir*, 14:5636–5648, 1998.

[18] Jeffrey N. Anker, W. Paige Hall, Olga Lyandres, Nilam C. Shah, Jing Zhao, and Richard P. Van Duyne. Biosensing with plasmonic nanosensors. *Nature Materials*, 7:442–453, 2008.

[19] Amanda J. Haes, Shengli Zou, George C. Schatz, and Richard P. Van Duyne. A nanoscale optical biosensor: The long range distance dependence of the localized surface plasmon resonance of noble metal nanoparticles. *The Journal of Physical Chemistry B*, 108(1):109–116, 2004.

[20] Amanda J. Haes, Shengli Zou, George C. Schatz, and Richard P. Van Duyne. Nanoscale optical biosensor: Short range distance dependence of the localized surface plasmon resonance of noble metal nanoparticles. *The Journal of Physical Chemistry B*, 108(22):6961–6968, 2004.

[21] Darya Radziuk and Helmuth Moehwald. Prospects for plasmonic hot spots in single molecule sers towards the chemical imaging of live cells. *Phys. Chem. Chem. Phys.*, 17:21072–21093, 2015.

[22] Dr. Abdennour Abbas, Dr. Limei Tian, Prof. Jeremiah J. Morrissey, Prof. Evan D. Kharasch, and Prof. Srikanth Singamaneni. Hot spot-localized artificial antibodies for label-free plasmonic biosensing. *Advanced functional materials*, 23:1789, 2013.

[23] Marek Piliarik and Jiří Homola. Surface plasmon resonance (spr) sensors: approaching their limits? *Optics Express*, 17:16505, 2009.

[24] Leiva Casemiro Oliveira, Antonio Marcus Nogueira Lima, Carsten Thirstrup, and Helmut Franz Neff. *Surface plasmon resonance sensors : a materials guide to design, characterization, optimization, and usage*. Springer, 2019.

[25] Xue Han, Kun Liu, and Changsen Sun. Plasmonics for biosensing. *Materials*, 12, 2019.

[26] Vasimalla Yesudasu, Himansu Shekhar Pradhan, and Rahul Jasvanthbhai Pandya. Recent progress in surface plasmon resonance based sensors: A comprehensive review. *Heliyon*, 7:e06321, 2021.

[27] Katherine A Willets and Richard P. Van Duyne. Localized surface plasmon reso-

nance spectroscopy and sensing. *Annual review of physical chemistry*, 58:267–297, 2007.

[28] Srdjan S. Acimovic, Maria A. Ortega, Vanesa Sanz, Johann Berthelot, Jose L. Garcia-Cordero, Jan Renger, Sebastian J. Maerkl, Mark P. Kreuzer, and Romain Quidant. Lspr chip for parallel, rapid, and sensitive detection of cancer markers in serum. *Nano Letters*, 14(5):2636–2641, 2014.

[29] Si Hoon Lee, Nathan C. Lindquist, Nathan J. Wittenberg, Luke R. Jordan, and Sang-Hyun Oh. Real-time full-spectral imaging and affinity measurements from 50 microfluidic channels using nanohole surface plasmon resonance. *Lab Chip*, 12:3882–3890, 2012.

[30] Laurent Feuz, Magnus P. Jonsson, and Fredrik Höök. Material-selective surface chemistry for nanoplasmonic sensors: Optimizing sensitivity and controlling binding to local hot spots. *Nano Letters*, 12(2):873–879, 2012.

[31] Jacqueline Ferreira, Marcos J. L. Santos, Mohammad M. Rahman, Alexandre G. Brolo, Reuven Gordon, David Sinton, and Emerson M. Girotto. Attomolar protein detection using in-hole surface plasmon resonance. *Journal of the American Chemical Society*, 131(2):436–437, 2009.

[32] John C. Hulteen and Richard P. Van Duyne. Nanosphere lithography: A materials general fabrication process for periodic particle array surfaces. *Journal of Vacuum Science and Technology A: Vacuum, Surfaces, and Films*, 13:1553, 1998.

[33] Christy L. Haynes and Richard P. Van Duyne. Nanosphere lithography: A versatile nanofabrication tool for studies of size-dependent nanoparticle optics. *The Journal of Physical Chemistry B*, 105(24):5599–5611, 2001.

[34] Ewelina Grabowska, Martyna Marchelek, Marta Paszkiewicz-Gawron, and Adriana Zaleska-Medynska. 3 - metal oxide photocatalysts. In Adriana Zaleska-Medynska, editor, *Metal Oxide-Based Photocatalysis*, Metal Oxides, pages 51–209. Elsevier, 2018.

[35] Stephanie Jung and Sven Diederichs. Isolation and differentiation of human macrophages view project identification and characterization of viability-associated long non-coding rnas in hepatocellular carcinoma view project. *Nature Cell Biology*, 11:228–234, 2009.

[36] He L, Thomson JM, Hemann MT, Hernando-Monge E, Mu D, Goodson S, Powers S, Cordon-Cardo C, Lowe SW, Hannon GJ, and Hammond SM. A microrna polycistron as a potential human oncogene. *Nature*, 435:828–833, 2005.

[37] Esquela-Kerscher A and Slack FJ. Oncomirs - micrornas with a role in cancer. *Nature reviews. Cancer*, 6:259–269, 2006.

[38] Gayatri K. Joshi, Samantha Deitz-McElyea, Merrell Johnson, Sonali Mali, Murray Korc, and Rajesh Sardar. Highly specific plasmonic biosensors for ultrasensitive microrna detection in plasma from pancreatic cancer patients. *Nano Letters*, 14:6955–6963, 2014.

[39] Andrey E. Miroshnichenko, Sergej Flach, and Yuri S. Kivshar. Fano resonances in

nanoscale structures. *Rev. Mod. Phys.*, 82:2257–2298, 2010.

[40] Alberto Biscontin, Silvia Casara, Stefano Cagnin, Lucia Tombolan, Angelo Rosolen, Gerolamo Lanfranchi, and Cristiano De Pittà. New mirna labeling method for bead-based quantification. *BMC Molecular Biology 2010 11:1*, 11:1–13, 2010.

[41] Li-Qun Gu, Meni Wanunu, Michael X. Wang, Larry McReynolds, and Yong Wang. Detection of mirnas with a nanopore single-molecule counter. *Expert review of molecular diagnostics*, 12:573, 2012.

[42] Shicai Xu, Jian Zhan, Baoyuan Man, Shouzhen Jiang, Weiwei Yue, Shoubao Gao, Chengang Guo, Hanping Liu, Zhenhua Li, Jihua Wang, and Yaoqi Zhou. Real-time reliable determination of binding kinetics of dna hybridization using a multi-channel graphene biosensor. *Nature Communications 2017 8:1*, 8:1–10, 2017.

[43] Park H, Germini A, Sforza S, Corradini R, Marchelli R, and Knoll W. Kinetic and affinity analyses of hybridization reactions between peptide nucleic acid probes and dna targets using surface plasmon field-enhanced fluorescence spectroscopy. *Biointerphases*, 1:113–122, 2006.

[44] Langmuir Irving. The adsorption of gases on plane surfaces of glass, mica and platinum. *Journal of the American Chemical Society*, 40(9):1361–1403, 1918.

[45] Huaying Zhao, Inna Gorshkova, Gregory Fu, and Peter Schuck. A comparison of binding surfaces for spr biosensing using an antibody–antigen system and affinity distribution analysis. *Methods (San Diego, Calif.)*, 59, 2012.

[46] Purushottam Babu Tiwari, Xuewen Wang, Jin He, and Yesim Darici. Analyzing surface plasmon resonance data: Choosing a correct biphasic model for interpretation. *Review of Scientific Instruments*, 86:035001, 2015.

[47] Schuck Peter and Zhao Huaying. The role of mass transport limitation and surface heterogeneity in the biophysical characterization of macromolecular binding processes by spr biosensing. *Methods in molecular biology (Clifton, N.J.)*, 627:15–54, 2010.

[48] Zhao Ming, Wang Xuefeng, and Nolte David. Mass-transport limitations in spot-based microarrays. *Biomedical optics express*, 1:983, 2010.

[49] Luka Vanjur, Thomas Carzaniga, Luca Casiraghi, Marcella Chiari, Giuliano Zanchetta, and Marco Buscaglia. Non-langmuir kinetics of dna surface hybridization. *Biophysical Journal*, 119(5):989–1001, 2020.